Geological Magazine

www.cambridge.org/geo

Neo-Tethyan subduction triggered Eocene–Oligocene magmatism in eastern Iran

Siavash Omidianfar[1], Iman Monsef[2], Mohammad Rahgoshay[1], Hadi Shafaii Moghadam[3], Brian Cousens[4], Ming Chen[5], Shahrokh Rajabpour[6] and Jianping Zheng[5]

[1]Faculty of Earth Sciences, Shahid Beheshti University, Tehran, Iran; [2]Department of Earth Sciences, Institute for Advanced Studies in Basic Sciences (IASBS), Zanjan 45137-66731, Iran; [3]School of Earth Sciences, Damghan University, Damghan 36716-41167, Iran; [4]Ottawa-Carleton Geoscience Centre, Department of Earth Sciences, Carleton University, 1125 Colonel By Drive, Ottawa, ON K1S 5B6, Canada; [5]School of Earth Sciences, State Key Laboratory of Geological Processes and Mineral Resources, China University of Geoscience, Wuhan, China and [6]Instituto de Geología Económica Aplicada (GEA), Universidad de Concepción, Casilla 160-C, Concepción, Chile

Original Article

Cite this article: Omidianfar S, Monsef I, Rahgoshay M, Shafaii Moghadam H, Cousens B, Chen M, Rajabpour S, and Zheng J (2023) Neo-Tethyan subduction triggered Eocene–Oligocene magmatism in eastern Iran. *Geological Magazine* **160**: 490–510. https://doi.org/10.1017/S0016756822001066

Received: 27 November 2021
Revised: 23 September 2022
Accepted: 26 September 2022
First published online: 14 December 2022

Keywords:
Cenozoic; magmatism; zircon U–Pb ages; Neo-Tethys; slab roll-back; Iranian Plateau; Sistan

Author for correspondence:
Siavash Omidianfar
Email: siavashomidianfar@gmail.com

Abstract

Eocene–Oligocene magmatic rocks are well exposed in the region south of Birjand, eastern Iran. The ages, geochemistry and petrogenesis of these rocks are important to understand eastern Iran's magmatic and geodynamic history during the Cenozoic. Detailed field investigations show that numerous intrusive, intermediate to felsic units are intruded into a thick sequence of Eocene–Oligocene lava flows and their accompanying pyroclastic rocks. The volcanic rocks are mainly basaltic andesitic to rhyolitic, whereas intrusive rocks are characterized by dioritic to granitic composition. Previously compiled U–Pb geochronological data indicate that Eocene–Oligocene magmatism in eastern Iran formed continuously from ~46 Ma to ~25 Ma. Our new zircon U–Pb data reveal crystallization ages of 43.6 ± 0.4 Ma to 39.5 ± 0.6 Ma, consistent with the upper end of this age range. Geochemically, the igneous rocks have high-K calc-alkaline to shoshonitic signatures. Rare-earth and trace element patterns show enrichment in LREEs, K, Rb, Cs, Pb, Th and U and depletion in HFSEs such as Nb, Zr and Ti, typical of a subduction-related environment. $^{87}Sr/^{86}Sr_{(i)}$ and $\epsilon Nd_{(i)}$ values range from 0.7051 to 0.7064 and −0.1 to +0.2, respectively. We postulate that the Cretaceous northeastward subduction of the Neo-Tethyan oceanic lithosphere underneath the Iranian Plateau caused sub-continental lithospheric mantle (SCLM) metasomatism by slab-derived fluid components. Subsequently, slab roll-back of the Neo-Tethyan oceanic lithosphere associated with asthenospheric upwelling led to lithospheric thinning and melting of the metasomatized SCLM. The resulting parental magmas probably interacted with upper continental crust during magma ascent to form Eocene–Oligocene magmatism in eastern Iran.

1. Introduction

Mesozoic and Cenozoic magmatic rocks are abundant in an elongated region from the west of Tauride–Anatolide to the Iranian Plateau and then to Afghanistan, Pakistan and Tibet in the east. The Iranian Plateau includes several continental fragments within the convergence zone of two rigid plates, the Arabian plate in the SW and the Eurasian plate in the NE (e.g. Hempton, 1978; Berberian 2014; Khodaverdian *et al.* 2015; see Fig. 1). The Iranian Plateau represents the second largest collisional system in elevation and size after the Tibetan Plateau (Paknia *et al.* 2021). During the Cenozoic, extensive magmatism occurred throughout the Iranian Plateau. This tremendous volume of magmatism is attributed to the NE-dipping subduction of the Neo-Tethyan oceanic lithosphere beneath the Iranian Plateau (e.g. Verdel *et al.* 2011; Chiu *et al.* 2013; Zhang *et al.* 2018). Cenozoic magmatism is mainly preserved in four different magmatic belts (Fig. 1): (a) the Urumieh–Dokhtar Magmatic Belt (UDMB), (b) the Alborz–Azerbaijan Magmatic Belt (AAMB), (c) the Northeast Iran Magmatic Belt (NEIMB) and (d) the Eastern Iran Magmatic Belt (EIMB). The UDMB is proposed to represent an Andean-type magmatic belt formed due to the subduction of Neo-Tethyan oceanic lithosphere beneath the Iranian Plateau (e.g. Omrani *et al.* 2008; Hassanzadeh & Wernicke 2016). However, rear-arc extensional magmatism was recently suggested to have formed the AAMB and NEIMB, caused by the slab roll-back of the Neo-Tethyan oceanic lithosphere (e.g. Sepidbar *et al.* 2019; Shafaii Moghadam *et al.* 2020).

The Cenozoic EIMB was built by various magmatic pulses, mainly during the Eocene to Oligocene, which are widespread in a roughly NW–SE-trending elongated belt (Fig. 1). It consists of a Palaeocene to Quaternary volcanic sequence (up to 2000 m thickness), which is intruded by numerous intermediate to felsic intrusions. Although the Eocene–Oligocene

© The Author(s), 2022. Published by Cambridge University Press.

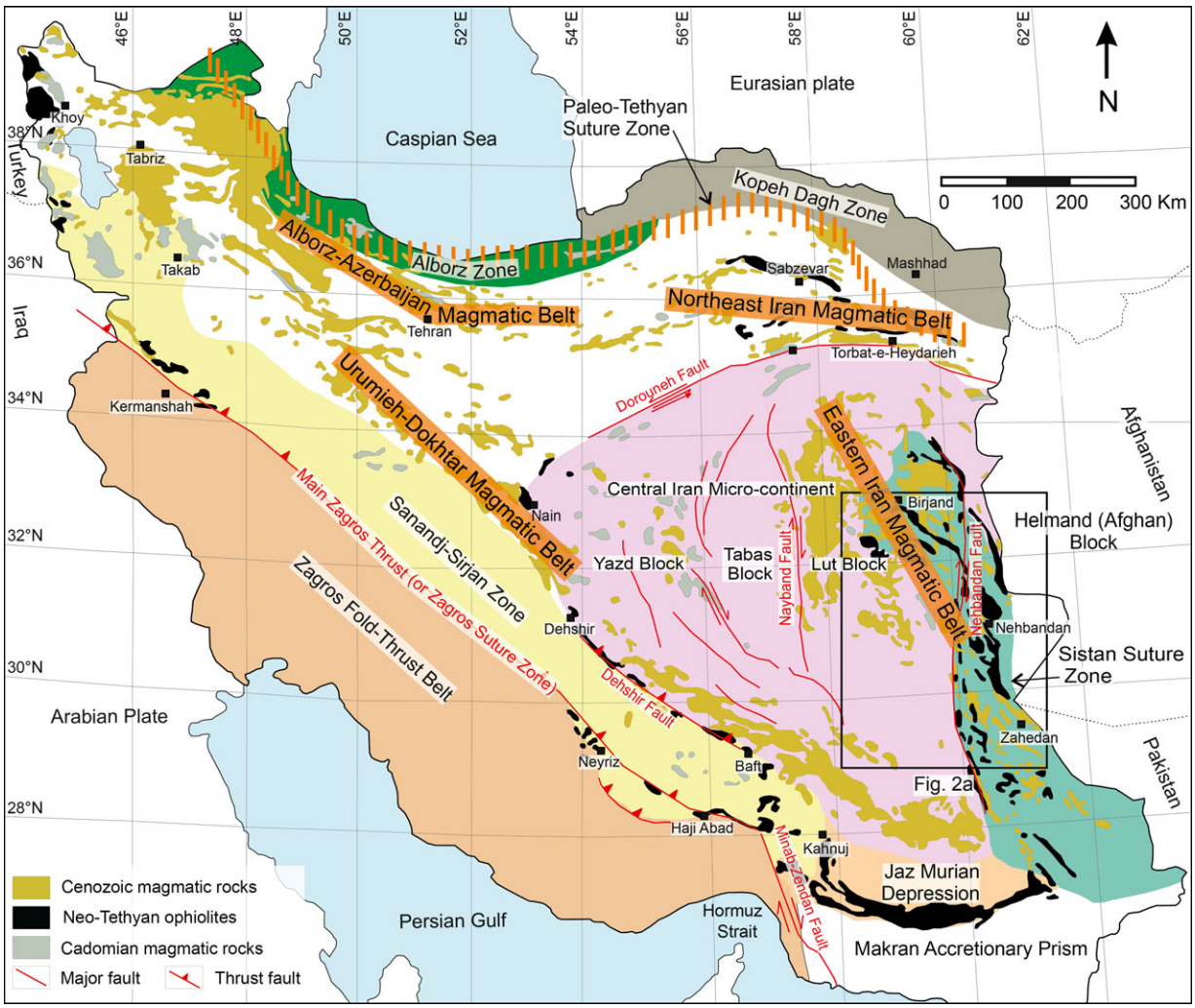


Fig. 1. (Colour online) A simplified geological map of Iran illustrates the distribution of four main magmatic belts: the Urumieh–Dokhtar, Alborz–Azerbaijan, Northeast Iran and Eastern Iran magmatic belts. Cadomian and Cenozoic magmatic rocks and Cretaceous Neo-Tethyan ophiolites are also shown (modified after Shafaii Moghadam *et al.* 2020). The Palaeo-Tethyan suture zone is from Rossetti *et al.* (2017). In this map, the term Iranian Plateau refers to an area between the Kopeh Dagh and Alborz Mountains in the north, the Zagros Fold-Thrust Belt in the west, the Persian Gulf and Hormuz Strait in the south and the Eastern Iranian Mountains in the east (Khodaverdian *et al.* 2015).

EIMB magmatism has been previously studied, there is still ongoing debate about source and formation mechanisms. For example, Verdel *et al.* (2011) suggested a subducting slab roll-back mechanism and an extensional tectonic setting to form the Eocene–Oligocene EIMB magmatic rocks. On the other hand, after the collision between the Lut and Afghan blocks, a post-collisional tectonic setting has been proposed to generate the EIMB igneous rocks (e.g. Pang *et al.* 2013; Sepidbar *et al.* 2018; Omidianfar *et al.* 2020). Alternatively, some studies attribute the EIMB magmatic rocks to an Andean-type active continental margin due to subduction of the Sistan Ocean underneath the Lut block (e.g. Arjmandzadeh *et al.* 2011; Beydokhti *et al.* 2015; Samiee *et al.* 2016; Nadermezerji *et al.* 2018).

We think there are ongoing challenges concerning mantle source compositions and magmatic evolution involved in forming the voluminous Eocene–Oligocene magmatism in eastern Iran. A further question is which geodynamic triggers could best explain the occurrence of this magmatic sequence. Herein, we report new field observations, zircon U–Pb ages and whole-rock major, trace and Sr–Nd isotope data for the intrusive rocks (Hanar intrusion) and volcanic sequences from the region south of Birjand. These data were compiled with previous geochemical data from the EIMB magmatic rocks to resolve ambiguities related to Eocene–Oligocene magmatism in eastern Iran.

2. Regional geology

The Cadomian crust of Iran (Ediacaran–Cambrian; see Fig. 1) is interpreted to have been produced by arc magmatism due to south-dipping subduction of proto-Tethys oceanic lithosphere beneath the northern margin of Gondwana (e.g. Rossetti *et al.* 2015; Shafaii Moghadam *et al.* 2015*a*). During the Permian to the Late Triassic, Cimmerian terranes, including the Iranian Plateau, drifted from Gondwana by rifting the Neo-Tethys Ocean behind it (e.g. Agard *et al.* 2011; Vergés *et al.* 2011). TheIranian Plateau was accreted to Eurasia during the Late Triassic to Early Jurassic, leading to the formation of the Palaeo-Tethyan suture zone (e.g. Stampfli *et al.* 1991; Zanchetta *et al.* 2013; Rossetti *et al.* 2017; see Fig. 1). Subsequently, northeastward subduction of the Neo-Tethys oceanic lithosphere beneath the Iranian Plateau was initiated in the Cretaceous and continued to the Eocene–Oligocene, leading to mantle metasomatism

https://doi.org/10.1017/S0016756822001066 Published online by Cambridge University Press

beneath the overriding plate (e.g. Shafaii Moghadam & Stern, 2021; Monsef *et al.* 2022). Neo-Tethyan ophiolites of Iran determine the location of ancient suture zones of the Iran–Cimmerian continental blocks (e.g. Khoy, Neyriz, Haji Abad, Birjand, Nain–Baft and Sabzevar ophiolites) (Shafaii Moghadam *et al.* 2009, 2015*b*; Monsef *et al.* 2010, 2014, 2018; Saccani *et al.* 2010; Zarrinkoub *et al.* 2012; see Fig. 1).

Eastern Iran is a geologically complex region and includes the Lut block and Sistan suture zone (Fig. 1). In the eastern part of the Central Iran micro-continent, the N–S-trending Lut block is bounded to the east by the Nehbandan Fault and Sistan suture zone, to the north by the Dorouneh Fault, to the west by the Nayband Fault, and to the south by the Jaz Murian depression. The Lut block consists of Cadomian, Mesozoic and Cenozoic magmatic rocks. The Sistan suture zone comprises Cretaceous flysch deposits (e.g. Babazadeh & De Wever, 2004; Bayet-Gol *et al.* 2016), high-pressure metamorphic rocks (e.g. Fotoohi Rad *et al.* 2005; Bröcker *et al.* 2013, 2022) and ophiolites (e.g. Nehbandan and Birjand ophiolites; Saccani *et al.* 2010; Zarrinkoub *et al.* 2012). The Sistan ophiolites represent the oceanic lithosphere, which existed between the Lut and Afghan blocks during the Late Mesozoic (Camp & Griffis, 1982; Tirrul *et al.* 1983). The age of the Sistan ocean is still debated, although radiolarites associated with ophiolitic lavas have Aptian–Albian ages (Babazadeh & De Wever, 2004). Furthermore, gabbroic rocks from the Birjand ophiolites yielded zircon U–Pb ages of 113 Ma to 104 Ma (Zarrinkoub *et al.* 2012; Bröcker *et al.* 2022). The closure time of the Sistan Ocean and the Lut–Afghan continental collision is controversial and considered to be Late Cretaceous (Babazadeh & De Wever, 2004; Saccani *et al.* 2010; Zarrinkoub *et al.* 2012; Angiboust *et al.* 2013), Middle Eocene (Camp & Griffis, 1982; Tirrul *et al.* 1983) or Oligocene – Middle Miocene (Şengör & Natal'in, 1996). In addition, based on the Rb–Sr dating of high-pressure metamorphic rocks (eclogites and blueschists) and zircon U–Pb ages of metafelsic rocks from the Birjand–Nehbandan ophiolites, Bröcker *et al.* (2013) suggested a Late Cretaceous age for the closing of the Sistan Ocean (89–83 Ma).

The EIMB comprises a large area, including the Lut block and Sistan suture zone (Figs 1, 2). Magmatic rocks within the EIMB include rare Cadomian felsic lavas and intrusions, Middle Jurassic felsic intrusive rocks, Late Cretaceous intermediate to felsic intrusive rocks and Late Cretaceous mafic to intermediate lavas and pyroclastic rocks. Palaeocene pyroclastic units cover the Late Cretaceous rocks. The Eocene–Oligocene magmatic rocks include mafic to felsic lava flows, pyroclastic rocks and intermediate to felsic intrusions. These rocks form a widespread and thick magmatic sequence in the EIMB. Miocene to Quaternary mafic lavas are the latest magmatic rocks within the EIMB (Fig. 2).

3. Geology of the study area

Our samples came from the region south of Birjand, covering an area of ~3000 km^2 (Fig. 3). The oldest rocks are Lower Jurassic shales, sandstones and limestones (Shemshak Fm.), intruded by Middle Jurassic granites. Upper Jurassic andesitic to dacitic lavas and pyroclastic rocks rest atop the Upper Jurassic limestones and sandy limestones. The Lower Palaeocene conglomerates stratigraphically cover the Lower to Upper Cretaceous flysch and turbidites. The Eocene to Oligocene extrusive and intrusive rocks are abundant, consisting of basaltic andesite to rhyolitic lava flows and pyroclastic rocks intruded by dioritic to granitic intrusions (Fig. 3).

Field observations indicate that the basaltic andesitic to rhyolitic lava flows have aphanitic to porphyritic textures and locally exhibit hydrothermal alteration, especially along fractures. Moreover, lava flows are associated with andesitic to rhyolitic tuffs and ignimbrites. The rhythmic association of lava flows and pyroclastic rocks suggests that the magmatic activities and eruptions are related to stratovolcanoes (Fig. 4a, b). In addition, several stock-like intrusive bodies (e.g. the Hanar pluton) are invaded into the Eocene–Oligocene volcanic rocks. The Hanar intrusive rocks are predominantly composed of diorites, quartz–diorites and granodiorites, although granites, monzodiorites and quartz–monzodiorites are rarely present (Fig. 4c, d). At contact with volcanic host rocks, the intrusive rocks are fine-grained (micro-diorite; Fig. 4c). Basaltic andesite to andesitic xenoliths (up to a few centimetres diameter) are locally found within the intrusive rocks (Fig. 4e).

4. Analytical techniques

We collected 180 samples of both intrusive (the Hanar pluton) and extrusive rocks from the region south of Birjand. The locations of representative magmatic rocks for geochronological and geochemical analyses are shown in Figure 2b. Sample locations, rock type and analytical methods are listed in the online Supplementary Material Table S1. Two samples from the Hanar pluton and two from the volcanic lavas were analysed for zircon U–Pb ages and trace elements by laser ablation – inductively coupled plasma – mass spectrometry (LA-ICP-MS; see online Supplementary Material Tables S2, S3). Based on petrographic characteristics, 22 of the freshest samples were analysed for whole-rock major and trace elements by X-ray fluorescence (XRF) and inductively coupled plasma – mass spectrometry (ICP-MS; see online Supplementary Material Table S4). In addition, five samples from the Hanar pluton and two from the volcanic lavas were selected for whole-rock Sr and Nd isotope analyses by thermal ionization mass spectrometry (TIMS; see online Supplementary Material Table S5). Analytical details are presented in the online Supplementary Material.

5. Results

5.a. Sample description

Intrusive rocks are mainly diorites, micro-diorites, quartz–diorites and granodiorites, although monzodiorites, quartz–monzodiorites and granites are also present. Diorites show granular texture and consist of subhedral to anhedral plagioclase and anhedral calcic-amphibole as significant phases. Fe–Ti oxides occur as an accessory phase (Fig. 5a). Optically (under the cross-polarized light), plagioclases have oligoclase to andesine composition. This has been inferred based on the extinction angles of the 'albite twins' of plagioclases and using the Michel–Levy technique (see Kerr, 1959, pp. 294–5). The presence of Oligoclase–andesine plagioclase, calcic-amphibole (instead of clinopyroxene) and the higher amounts of SiO_2 (54.97 to 59.97 wt. %) than gabbroic rocks confirm these rocks have an intermediate dioritic composition (see Figs 5a and (further below) 8). Micro-diorites are porphyritic and contain subhedral plagioclase, anhedral calcic-amphibole and subhedral to anhedral clinopyroxene phenocrysts in a fine-grained groundmass of plagioclase, calcic-amphibole, quartz and Fe–Ti oxides (online Supplementary Material Fig. S1a, b). Quartz–diorites have granular and myrmekitic textures (Fig. 5b), with moderately altered

https://doi.org/10.1017/S0016756822001066 Published online by Cambridge University Press

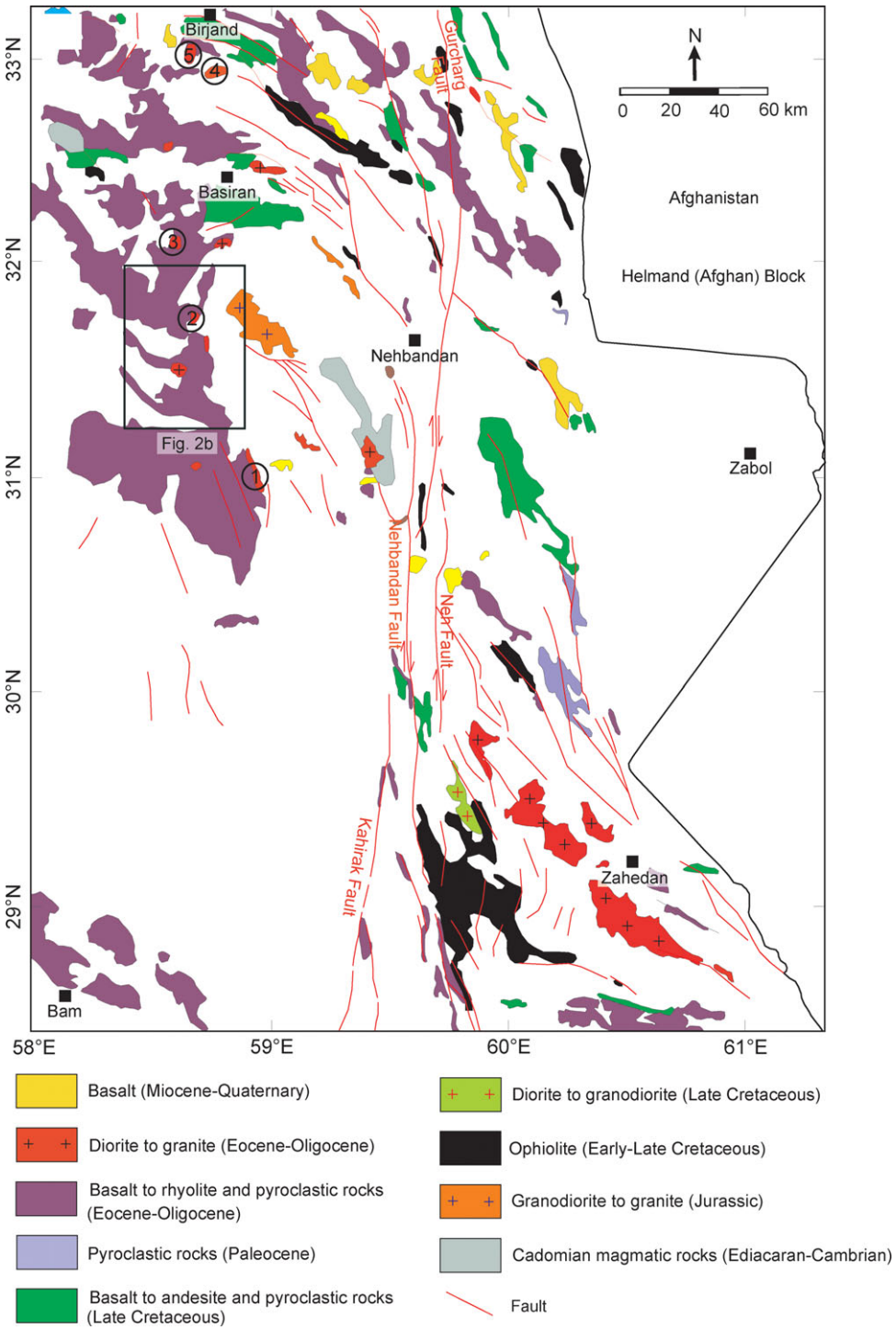


Fig. 2. (Colour online) Simplified magmatic map of eastern Iran (modified after Emami *et al.* 1993). Circles with numbers indicate the Eocene–Oligocene intrusions of the EIMB used for comparison. Numbers correspond to (1) Mahoor intrusion (31.9 ± 0.2 Ma; Beydokhti *et al.* 2015); (2) Chah-Shaljami intrusion (33.5 ± 1 Ma; Arjmandzadeh *et al.* 2011); (3) Koudakan intrusion (37.9 ± 0.8 to 41.7 ± 3.4 Ma; Omidianfar *et al.* 2020); (4) Khunik intrusion (38 ± 1 Ma; Samiee *et al.* 2016); and (5) Shah-Soltan Ali intrusion (38.3 ± 0.5 Ma; Nadermezerji *et al.* 2018).

plagioclase and quartz as significant phases and calcic-amphibole as a minor constituent. Monzodiorites and quartz–monzodiorites have a granular texture. They are composed mainly of plagioclase and alkali feldspar and a variable amount of quartz (<5 % in monzodiorites, to >5 but <10 % in quartz–monzodiorites). The minor phases are calcic-amphibole, biotite and Fe–Ti oxides (online Supplementary Material Fig. S1c). Granodiorites and granites have a granular texture with anhedral quartz, subhedral to anhedral plagioclase and anhedral alkali feldspar as major components (alkali feldspar > plagioclase in granites) associated with calcic-amphibole and biotite as minor constituents (online Supplementary Material Fig. S1d).

Volcanic rocks include basaltic andesites, andesites, trachyandesites, quartz–trachyandesites, trachytes, quartz–trachytes, dacites, rhyodacites and rhyolites. They mostly show porphyritic and glomeroporphyritic textures with micro- to crypto-crystalline and rarely glassy groundmass. Basaltic andesites have subhedral plagioclase (up to 20 %) and subhedral to anhedral clinopyroxene (up to 5 %) phenocrysts. The groundmass of these rocks contains clinopyroxene, calcic-amphibole, plagioclase laths and Fe–Ti

https://doi.org/10.1017/S0016756822001066 Published online by Cambridge University Press

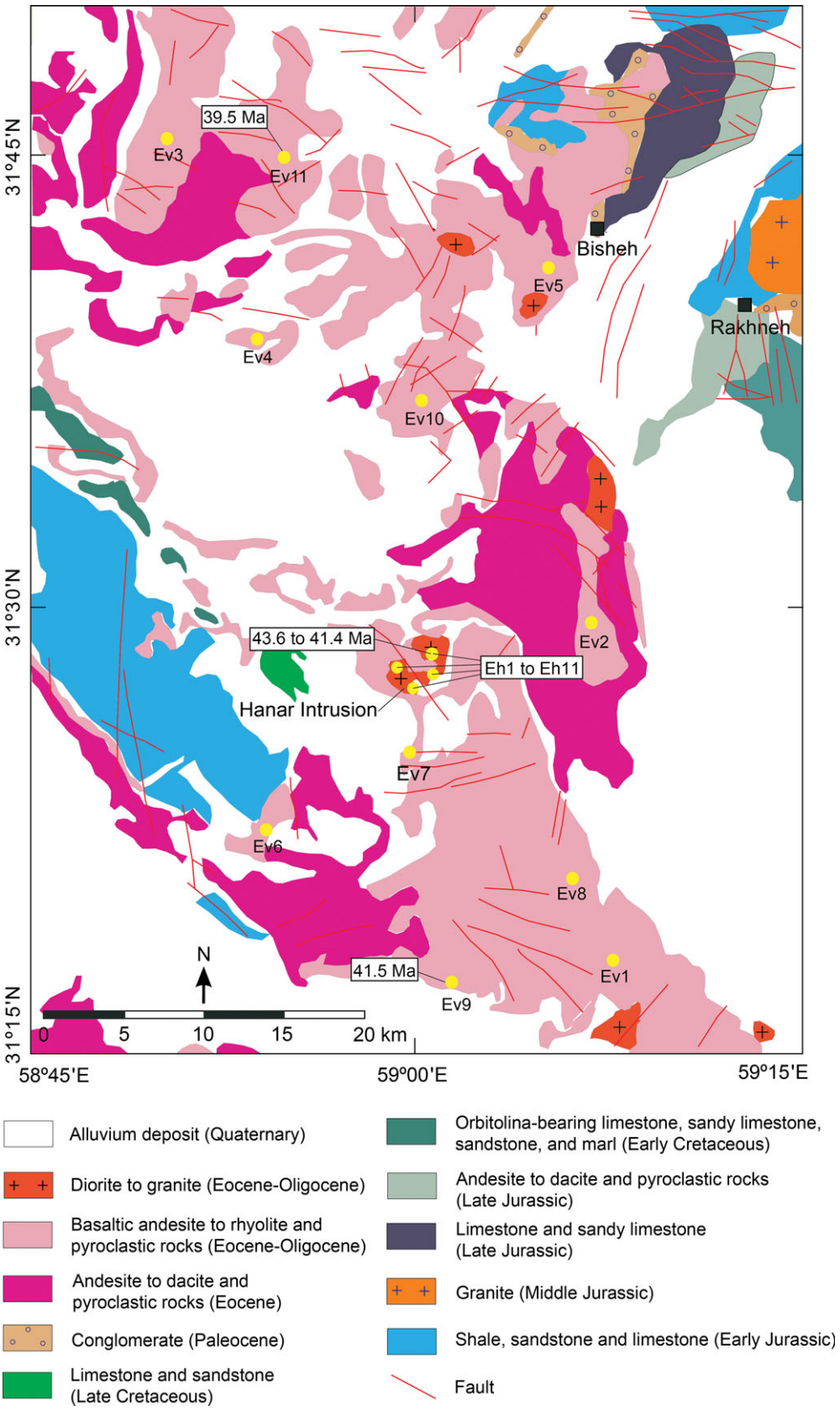


Fig. 3. (Colour online) Geological map of the region south of Birjand, showing the distribution of extrusive rocks and Hanar intrusive rocks (modified after Sahandi, 1992). Yellow circles indicate the geographical locations of the newly analysed samples.

oxides (Fig. 5c, d). Andesites include euhedral to subhedral plagioclase (up to 20 %), euhedral to anhedral calcic-amphibole (up to 20 %) phenocrysts and microphenocrysts, and a groundmass consisting of plagioclase laths, calcic-amphibole and Fe–Ti oxides (online Supplementary Material Fig. S2a, b). Some plagioclase phenocrysts show sieve texture, indicating rapid decompression

https://doi.org/10.1017/S0016756822001066 Published online by Cambridge University Press

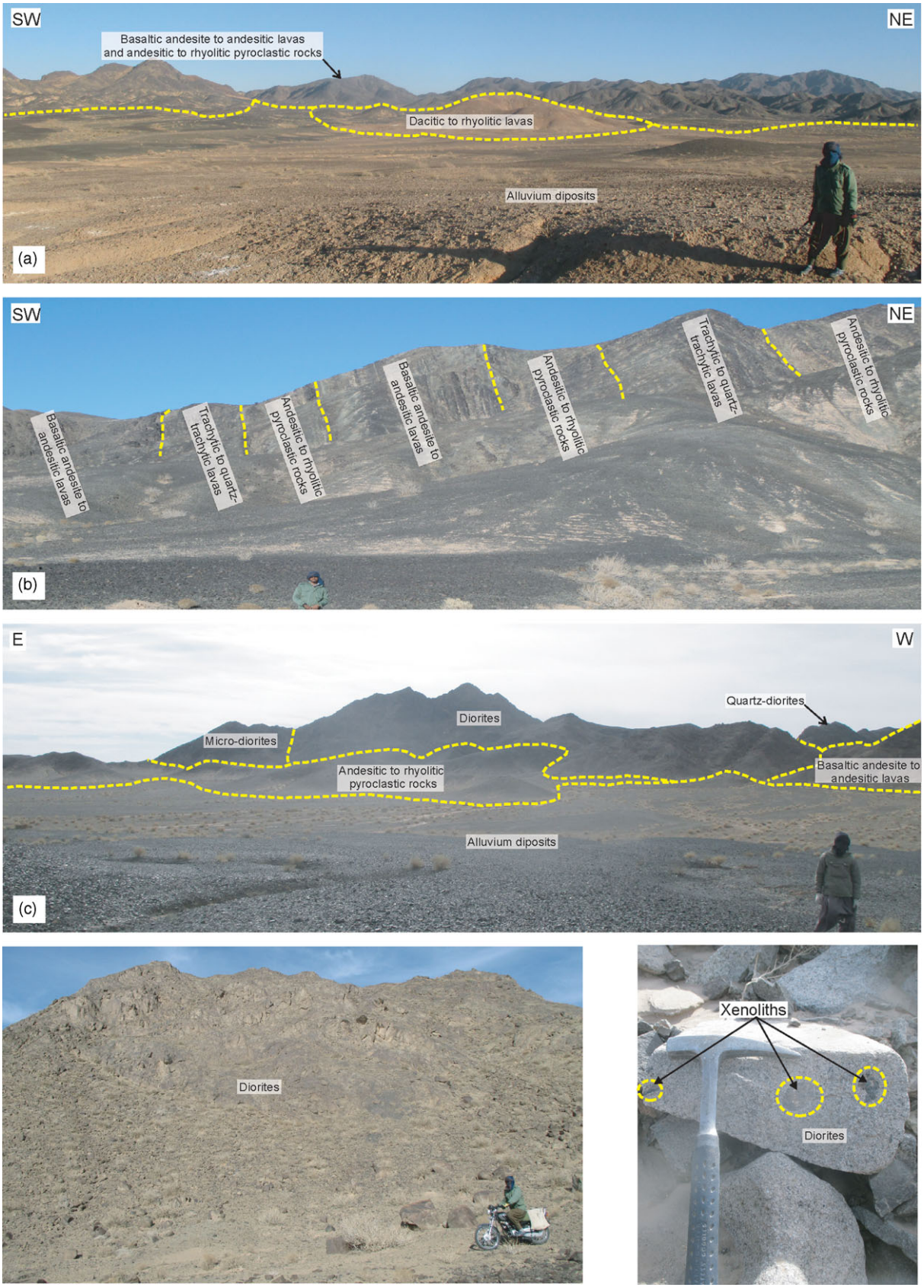


Fig. 4. (Colour online) Field photographs from the magmatic rocks of the region south of Birjand. (a) An outcrop of basaltic andesite to rhyolitic lava flows and pyroclastic rocks. (b) A sequence of basaltic andesite to rhyolitic lavas and pyroclastic rocks. (c) An overview of dioritic and quartz–dioritic intrusive rocks injected within the lavas and pyroclastic rocks. (d) A close-up view of the Hanar dioritic intrusive rocks. (e) Xenoliths within dioritic rocks. Yellow dashed lines show lithological boundaries.

https://doi.org/10.1017/S0016756822001066 Published online by Cambridge University Press

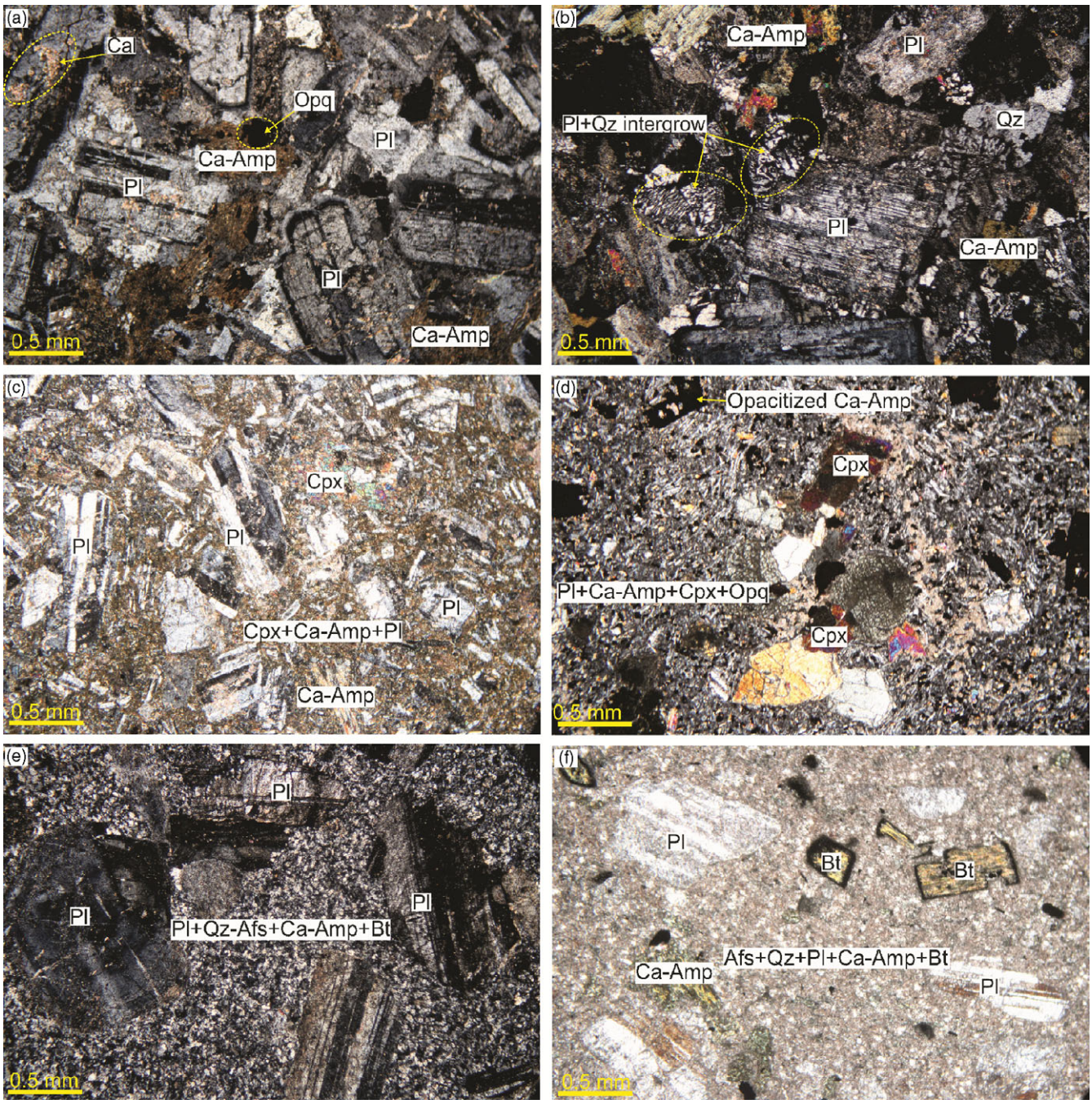


Fig. 5. (Colour online) Photomicrographs from the magmatic rocks of the region south of Birjand. (a) Diorites with a granular texture, consisting of plagioclase and calcic-amphibole. (b) Quartz–diorites with granular and myrmekite texture (Pl–Qz intergrowth), including plagioclase, quartz and calcic-amphibole. (c) Basaltic andesite with porphyritic texture, consisting of plagioclase and clinopyroxene as phenocrysts in a fine-grained groundmass of clinopyroxene, calcic-amphibole and plagioclase. (d) Basaltic andesites with glomeroporphyritic texture, containing clinopyroxene and opacitized calcic-amphibole phenocrysts within a groundmass of plagioclase laths, calcic-amphibole, clinopyroxene and Fe–Ti oxides. (e) Dacites with porphyritic texture, outlining plagioclase phenocrysts in a fine-grained groundmass of alkali feldspar, plagioclase, quartz, calcic-amphibole and biotite. (f) Rhyodacites with porphyritic texture, highlighting plagioclase, calcic-amphibole and opacitized biotite phenocrysts within a groundmass of alkali feldspar, plagioclase, quartz, calcic-amphibole and biotite. Abbreviations; Pl: plagioclase; Afs: alkali feldspar; Qz: quartz; Cpx: clinopyroxene; Ca-Amp: calcic-amphibole; Bi: biotite; Cal: calcite; Opq: opaque minerals (Whitney & Evans, 2010). Scale bars are 0.5 mm across. Photos were taken using crossed-polarized light (XPL).

during magma ascent or magma mixing. Trachyandesites and quartz–trachyandesites contain calcic-amphibole (up to 10 %) and plagioclase (up to 3 %) phenocrysts in a groundmass of plagioclase, alkali feldspar, calcic-amphibole, quartz and Fe–Ti oxides (online Supplementary Material Fig. S2c). Trachytes and quartz–trachytes include alkali feldspar (up to 10 %), plagioclase (up to 5 %) and biotite (up to 5 %) phenocrysts in a groundmass of plagioclase and alkali feldspar microlites, biotite, quartz and Fe–Ti oxides. Dacites, rhyodacites and rhyolites consist of variable amounts of plagioclase (up to 20 %), alkali feldspar (up to 10 %), quartz (up to 10 %), calcic-amphibole (up to 5 %) and biotite (up to 3 %) phenocrysts in a cryptocrystalline groundmass. Fe–Ti oxides are accessory minerals (Fig. 5e, f and online Supplementary Material Fig. S2d).

https://doi.org/10.1017/S0016756822001066 Published online by Cambridge University Press



Fig. 6. (Colour online) Cathodoluminescence (CL) images for zircons from the magmatic rocks of the region south of Birjand. Circles indicate the position of laser spots for zircon U–Pb analyses. Analytical numbers and $^{206}Pb/^{238}U$ ages are also shown. Scale bars are 100 μm across.

5.b. Zircon U–Pb geochronology and trace element geochemistry

Four samples were selected for zircon U–Pb dating (online Supplementary Material Table S2), including one diorite (sample Eh10), one granodiorite (sample Eh11) and two dacites (samples Ev9 and Ev11). Also, zircon grains from these samples were further analysed for trace elements (online Supplementary Material Table S3). In cathodoluminescence (CL) images (Fig. 6), zircon grains are euhedral to subhedral and prismatic, with lengths ranging from 50 to 250 μm. While most of the investigated zircon crystals in Fig. 6 exhibit oscillatory zoning, some zircon grains have complex internal textures of convoluted zoning and unzoned rims/domains. In chondrite-normalized rare earth element (REE) patterns, zircon grains display depletion in the light rare earth elements (LREEs) relative to the heavy rare earth elements (HREEs), negative Eu and positive Ce anomalies (online Supplementary Material Fig. S3). Moreover, the Th/U ratio of the analysed zircon grains ranges from 0.6 to 2.3, which is higher than those commonly found in metamorphic rocks (<0.1) (e.g. Rubatto *et al.* 2001). Finally, all

https://doi.org/10.1017/S0016756822001066 Published online by Cambridge University Press

trace element features support the interpretation that the zircons crystallized from magmatic liquids (Hoskin, 1998; Wu & Zheng, 2004; Corfu *et al.* 2003).

A total of 28 U–Pb analyses were performed on diorite sample Eh10. On a Tera–Wasserburg plot ($^{207}Pb/^{206}Pb$ vs $^{238}U/^{206}Pb$; see Fig. 7a), 20 analyses define an intercept age of 43.5 ± 0.4 Ma (MSWD = 2.6). The weighted mean age of zircons is 43.6 ± 0.4 Ma (MSWD = 1; $n = 20$). This weighted mean age is interpreted as the crystallization age of the diorite. Two zircon grains yielded older $^{206}Pb/^{238}U$ ages 114 Ma and 61 Ma, representing xenocrysts inherited from older country rocks.

A total of 24 zircon grains were analysed from a granodiorite sample Eh11. In a Tera–Wasserburg diagram (Fig. 7b), 11 grains have an intercept age of 41.2 ± 0.4 Ma (MSWD = 1.7). Zircon grains yielded a weighted mean age of 41.4 ± 0.5 Ma (MSWD = 1.5; $n = 15$), indicating the granodiorite's crystallization age. Five zircons show older $^{206}Pb/^{238}U$ ages of 164 Ma, 108 Ma, 78 Ma, 70 Ma and 56 Ma, which are inherited.

A total of 15 analyses were carried out on a dacite sample Ev9. On a Tera–Wasserburg plot (Fig. 7c), ten zircon grains display an intercept age of 41.5 ± 0.5 Ma (MSWD = 1.5) with an identical weighted mean age of 41.5 ± 0.5 Ma (MSWD = 0.87; $n = 10$). This age is interpreted as the age of dacite crystallization.

Finally, 15 zircon grains were analysed from a dacite sample Ev11. In a Tera–Wasserburg diagram (Fig. 7d), ten analysed zircons gave an intercept age of 39.8 ± 0.8 Ma (MSWD = 2.3) with a weighted mean age of 39.5 ± 0.6 Ma (MSWD = 1.5; $n = 10$). This weighted mean age is interpreted as the crystallization age of the dacite. The data point with the oldest $^{206}Pb/^{238}U$ age of 439 Ma represents a xenocryst.

5.c. Whole-rock major and trace element geochemistry

Whole-rock major and trace element analyses of the intrusive and extrusive rocks are reported in the online Supplementary Material Table S4. In the analysed samples, loss on ignition (LOI) values are low and range from 1.11 to 2.98 %. Because the LOI abundances are low, major elements have not been recalculated to 100 % volatile-free. In the total alkalis ($Na_2O + K_2O$) vs silica (SiO_2) classification diagram (TAS), the extrusive rocks fall in the basaltic trachyandesite, trachyandesite, andesite, trachyte, dacite and rhyolite domains (Fig. 8). In addition, the intrusive samples mainly plot in the fields of diorite and granodiorite (Fig. 7). In the Harker variation diagrams (Fig. 8), the intrusive samples reveal trends expected for magmatic fractionation of Ca-rich plagioclase, clinopyroxene, calcic-amphibole (hornblende), Fe–Ti oxide and apatite. The similarity in trends between the extrusive and intrusive rocks reveals their co-genetic nature and probable crystallization from the same parental magmas (Fig. 9). In the K_2O vs SiO_2 diagram (Fig. 10a), the intrusive and extrusive samples mostly trend to the high-K calc-alkaline and shoshonitic series. Furthermore, in the $Na_2O + K_2O$ – CaO vs SiO_2 diagram, the samples predominantly indicate calcic to calcic-alkalic affinities (Fig. 10b). The A/CNK (molar $Al_2O_3/(CaO + Na_2O + K_2O)$ vs A/NK (molar $Al_2O_3/(Na_2O + K_2O)$ diagram shows that the magmatic rocks belong to metaluminous and I-type granitoids (Fig. 10c). The presence of biotites, hornblendes and Fe–Ti oxides in these samples further attests to the I-type geochemical signature (Chappell & White, 2001). The $FeO_{total}/(FeO_{total} + MgO)$ vs SiO_2 diagram (Fig. 10d) displays a magnesian characteristic for these rocks similar to Cordilleran I-type granitoids.

In chondrite-normalized REEs diagrams (Fig. 11a, c), the magmatic rocks exhibit slight to moderate LREE enrichment relative to HREE. La_N/Yb_N varies from 2.75 to 6.45 in the intrusive rocks and 2.53 to 16.55 in the extrusive rocks. Most REE patterns show negative anomalies in Eu (Eu/Eu* = 0.56–0.98), indicating moderate plagioclase removal (Henderson, 1983). In primitive-mantle-normalized multi-element diagrams (Fig. 11b, d), the intrusive and extrusive rocks are characterized by enrichment in large-ion lithophile elements (LILEs) such as Cs, Rb, Ba, K, Sr and Pb as well as Th and U, and depletion in high-field-strength elements (HFSEs) such as Nb, Zr and Ti. In the magmatic rocks, the Nb_N/La_N ratios range from 0.31 to 0.71, and the Th_N/La_N ratios vary from 1.41 to 11.19. In the Nb vs Y diagram (Fig. 12a), the intrusive and extrusive samples plot within the volcanic arc granite plus syn-collisional granite domain. The Rb vs Y + Nb diagram further attests to these being volcanic arc granite (Fig. 12b). Likewise, in the Nb/Zr vs Zr diagram (Fig. 12c), the intrusive and extrusive rocks indicate subduction-related rather than collisional or intraplate settings. Moreover, in the Th/Yb vs Ta/Yb diagram (Fig. 12d), the magmatic rocks have high Th/Yb ratios, similar to those that erupted in active continental margins.

5.d. Whole-rock Sr–Nd isotope geochemistry

The age-corrected, initial ($_i$) Sr–Nd isotopic compositions of the igneous rocks from the target area in the EIMB are listed in the online Supplementary Material Table S5. The $^{87}Sr/^{86}Sr_{(i)}$ ratios range from 0.7061 to 0.7064, and $\epsilon Nd_{(i)}$ values vary from −1.6 to −0.1 in the intrusive rocks. In the extrusive rocks, the $^{87}Sr/^{86}Sr_{(i)}$ ratios range from 0.7051 to 0.7052 and $\epsilon Nd_{(i)}$ values vary from −0.1 to +0.2. The Nd model ages (T_{DM}) for the intrusive rocks range from 0.80 to 1.6 Ga, while the Nd model ages vary from 0.87 to 0.88 Ga in the extrusive rocks. In the $^{143}Nd/^{144}Nd_{(i)}$ vs $^{87}Sr/^{86}Sr_{(i)}$ plot (Fig. 13a), the Eocene–Oligocene EIMB igneous rocks are isotopically different from magmatic rocks formed from melting of a depleted MORB-type mantle (DMM) and plot between the end-members of DMM and enriched mantle components (EMI and EMII).

6. Discussion

6.a. Age, origin and magmatic evolution of the Eocene–Oligocene EIMB igneous rocks

Several studies looked at the geochronology and geochemistry of the Eocene–Oligocene EIMB igneous rocks. Available ages, geochemical characteristics and tectono-magmatic settings for different magmatic rocks within the EIMB are presented in Table 1. The new zircon U–Pb ages from the extrusive (41.5 ± 0.5 Ma to 39.8 ± 0.8 Ma) and intrusive (43.5 ± 0.4 Ma to 41.2 ± 0.4 Ma) rocks are consistent with ages reported by Pang *et al.* (2013) for other EIMB magmatic rocks (~46 Ma to ~25 Ma). Notably, our zircon U–Pb ages for the intrusive rocks are slightly older than those of the extrusive rocks. Our dated extrusive rocks appear to represent only a small fraction of the lengthy volcanic activity in eastern Iran, and they are not in direct contact with the older intrusive rocks (the Hanar intrusion; see Fig. 3). This thick volcanic sequence was intruded by numerous intrusive bodies (Fig. 2) with different ages such as the Hanar (43.5 ± 0.4 Ma to 41.2 ± 0.4 Ma), Mahoor (31.9 ± 0.2 Ma; Beydokhti *et al.* 2015), Chah-Shaljami (33.5 ± 1 Ma; Arjmandzadeh *et al.* 2011), Koudakan (37.9 ± 0.8 to 41.7 ± 3.4 Ma; Omidianfar *et al.* 2020), Khunik (38 ± 1 Ma;

https://doi.org/10.1017/S0016756822001066 Published online by Cambridge University Press

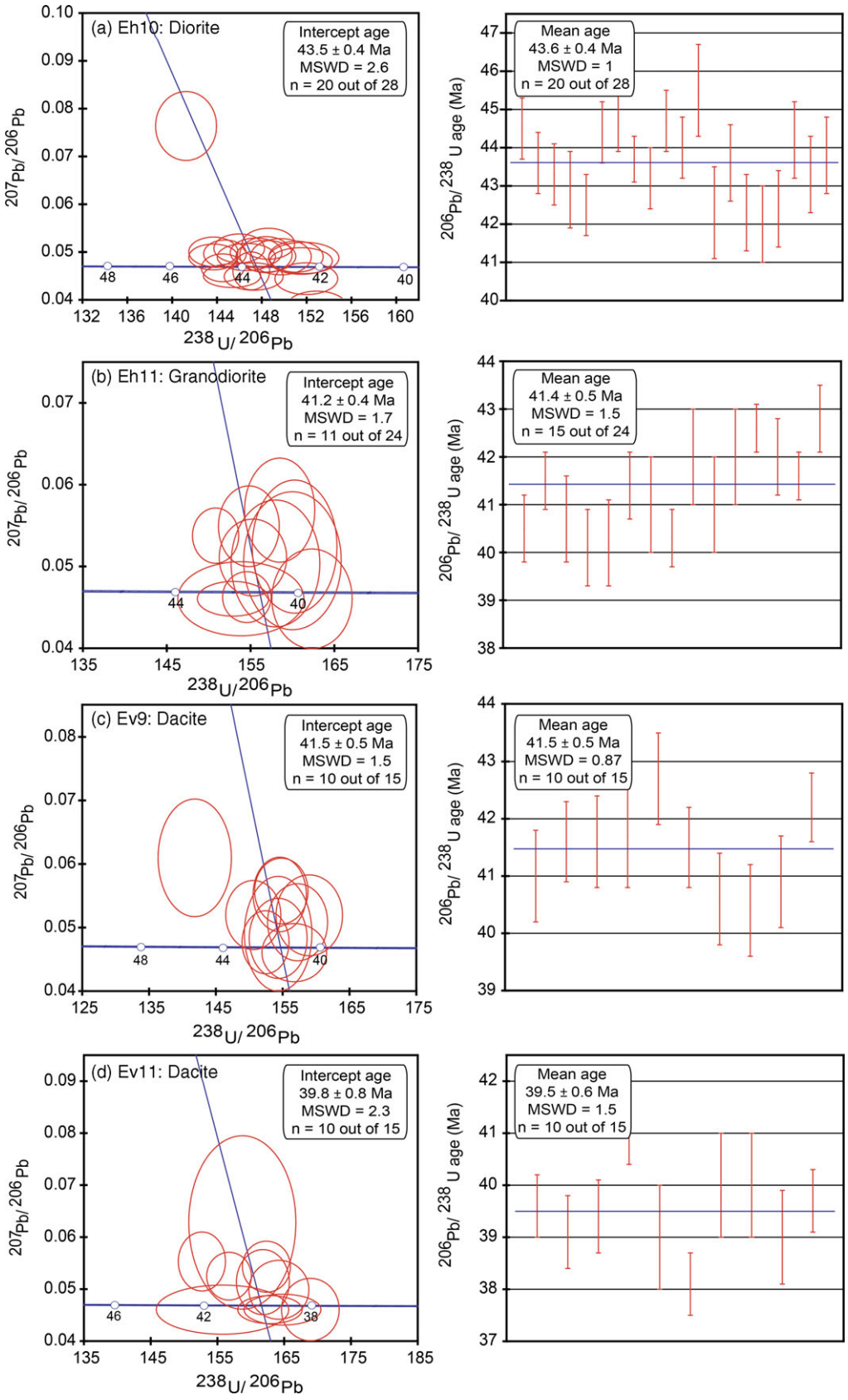


Fig. 7. (Colour online) U–Pb Tera–Wasserburg diagrams of $^{238}U/^{206}Pb$ vs $^{207}Pb/^{206}Pb$ and weighted mean ages of $^{206}Pb/^{238}U$ for zircons from the magmatic rocks of the region south of Birjand. Data-point error ellipses display 1σ uncertainties. Intercept ages are based on a mixing trend with a common Pb composition (Stacey & Kramers, 1975) anchored at $^{207}Pb/^{206}Pb$ values of 0.838, representing $t = 40$ Ma. The number of analysed zircons and those used for making the Tera–Wasserburg diagrams are reported in all plots. All red circles and bars are data used for calculating the intercept and weighted mean ages.

https://doi.org/10.1017/S0016756822001066 Published online by Cambridge University Press

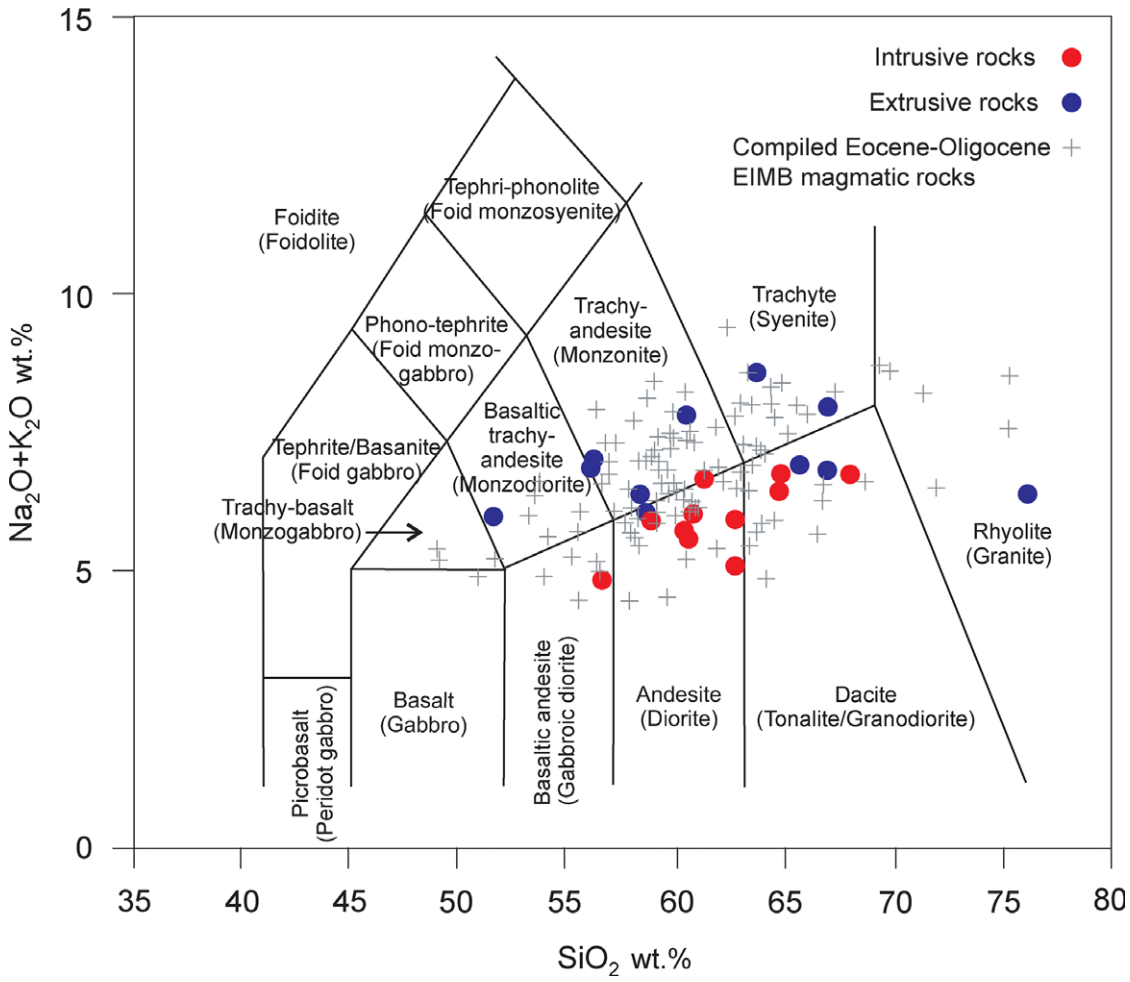


Fig. 8. (Colour online) Classification diagram of $Na_2O + K_2O$ (wt %) vs SiO_2 (wt %) (Middlemost, 1994) for the EIMB magmatic rocks. All oxides are calculated as anhydrous. Data sources for the compiled Eocene–Oligocene EIMB magmatic rocks are: Mahoor intrusion, Beydokhti *et al.* (2015); Chah-Shaljami intrusion, Arjmandzadeh *et al.* (2011); Koudakan intrusion, Omidianfar *et al.* (2020); Khunik intrusion, Samiee *et al.* (2016); Shah-Soltan Ali intrusion, Nadermezerji *et al.* (2018); and extrusive rocks, Pang *et al.* (2013).

Samiee *et al.* 2016) and Shah-Soltan Ali (38.3 ± 0.5 Ma; Nadermezerji *et al.* 2018) intrusions.

According to new and compiled geochemical data, enrichment in the LREEs and LILEs relative to the HREEs and HFSEs and high-K calc-alkaline to shoshonitic affinities of the Eocene–Oligocene EIMB igneous rocks (Figs. 10, 11) suggest that these rocks were derived from a LILE-metasomatized mantle source. The normalized REE and trace element patterns are mainly controlled by fluids/melts released from the subducting slab into the mantle wedge (Pearce *et al.* 2005; Tatsumi, 2005). Furthermore, the Eocene–Oligocene EIMB igneous rocks mainly indicate similarities to subduction-related settings (Fig. 12a–c) and have high Th/Yb and Ta/Yb ratios (Fig. 12d), indicating they likely originated from an enriched mantle source modified by slab-derived components. Notably, subduction-related metasomatism in the source rocks of the Eocene–Oligocene EIMB magmatic rocks is supported by their Sr–Nd isotopic values in that they have high $^{87}Sr/^{86}Sr_{(i)}$ at a given $\epsilon Nd_{(i)}$ due to the addition of seawater-derived Sr (Willbold & Stracke, 2010) (Fig. 13).

The high-K subduction-related magmas could have been derived from several potential sources, including: (i) by partial melting of a peridotite driven by the addition of fluids/melts released from a deeply subducted slab into the mantle wedge (Avanzinelli *et al.* 2009); (ii) partial melting (remelting) of calc-alkaline and subduction-related mafic rocks from the lower continental crust (Hou *et al.* 2004); (iii) magma mixing and crustal contamination (Mamani *et al.* 2008); and (iv) lower crustal assimilation in MASH (Melting Assimilation Storage Homogenization) or Hot Zones (Annen *et al.* 2006).

The Mg# (40.4–62.1), Cr (22–166 ppm) and Ni (10–62 ppm) concentrations in the magmatic rocks of this study (online Supplementary Material Table S4) are much lower than values for mantle (peridotite)-derived primitive melts (Mg# = 73–81, Cr > 1000 ppm and Ni > 400 ppm; Wilson, 1989). The Y/Nb, Nb/Ta and Zr/Nb ratios are unaffected by fractionation, so they can help identify the EIMB magma source (Eby, 1992; Thieblemont & Tegyey, 1994; Green, 1995; Morata *et al.* 2005). For example, the Y/Nb ratio in mantle-derived melts is <1.2, whereas this ratio is >1.2 in crustal-derived melts (Eby, 1992). The Y/Nb ratio in our EIMB magmatic rocks varies from 1.2 to 3.66 (online Supplementary Material Table S4). Green (1995) noted that the average Nb/Ta ratio is ~17.5 in mantle-derived melts and ~11.5 in crustal-derived melts. This ratio ranges from 5.37 to 11.67 in the igneous rocks of this study (online Supplementary Material Table S4). The Zr/Nb ratio could also be representative, ranging from 6.3 to 7.6 in mantle-derived melts and 22 to 25 in crustal-derived melts (Morata *et al.* 2005). This ratio ranges from 1.6 to 16.9 in the EIMB magmatic rocks (online Supplementary

https://doi.org/10.1017/S0016756822001066 Published online by Cambridge University Press

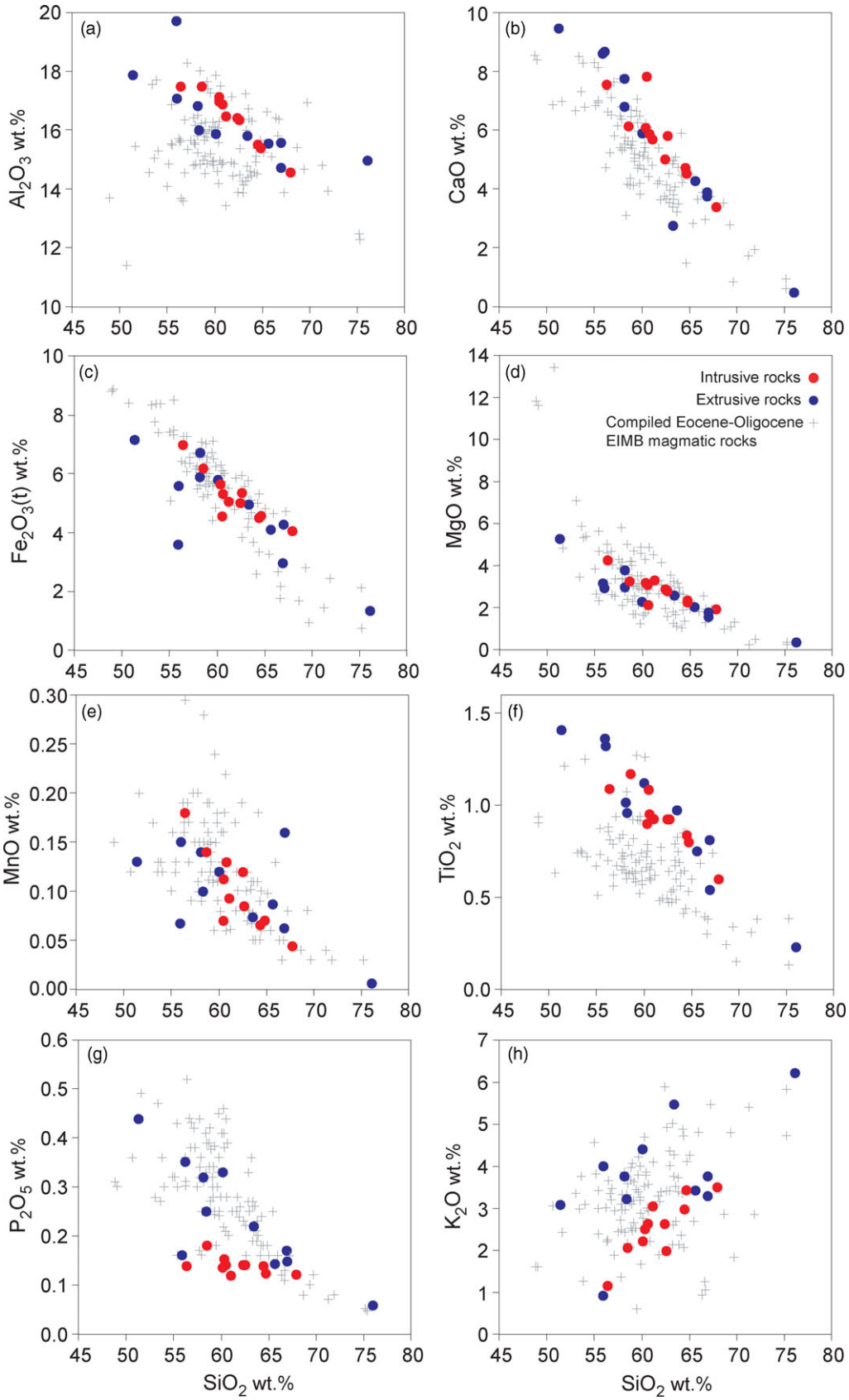


Fig. 9. (Colour online) Harker variation diagrams of major element oxides (wt %) against SiO_2 (wt %) for the EIMB magmatic rocks. All oxides are calculated as anhydrous. Data sources for the compiled Eocene–Oligocene EIMB igneous rocks are listed in Figure 8.

https://doi.org/10.1017/S0016756822001066 Published online by Cambridge University Press

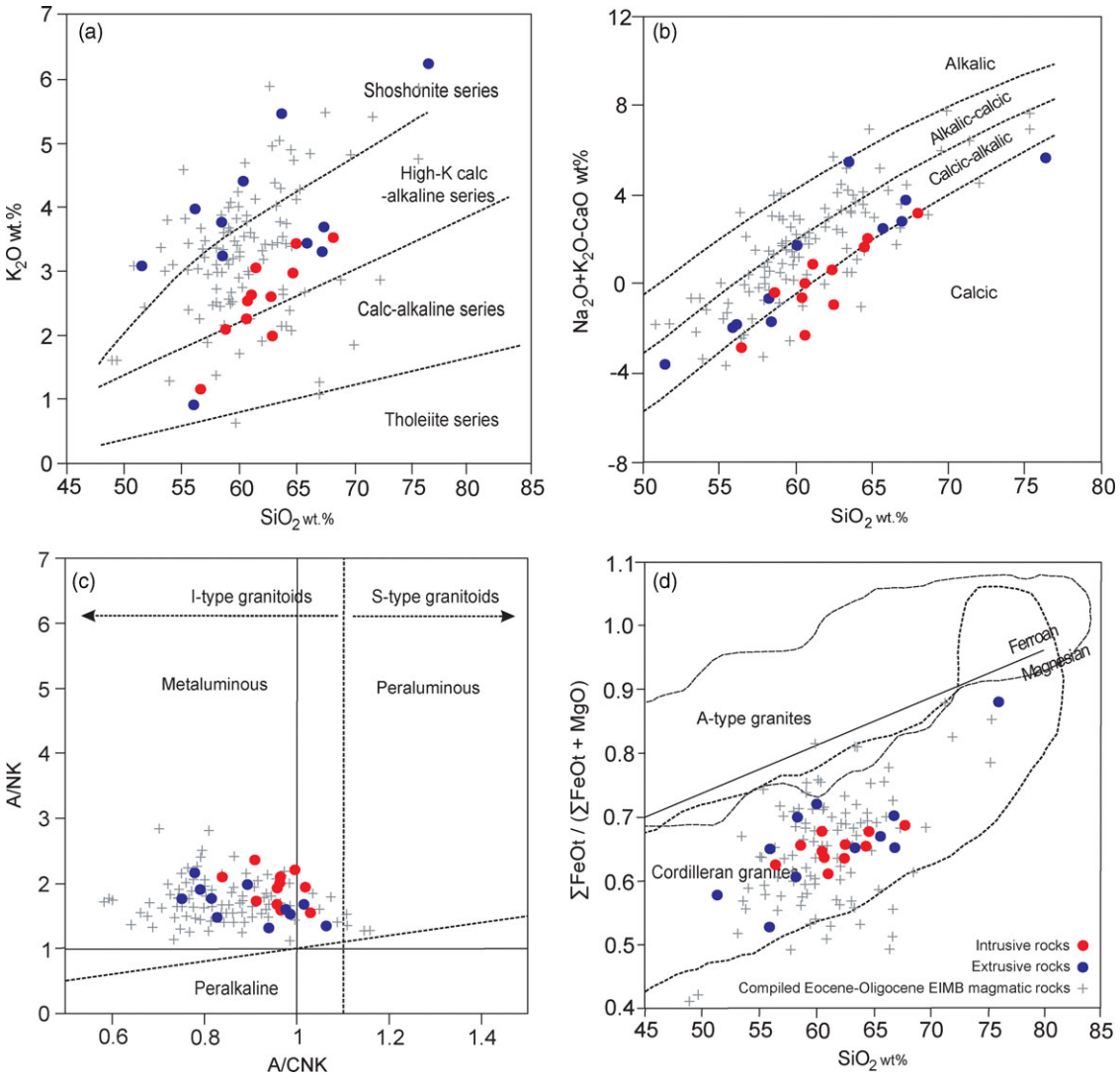


Fig. 10. (Colour online) Geochemical discrimination diagrams for the EIMB magmatic rocks. (a) A plot of K_2O (wt %) vs SiO_2 (wt %) (Peccerillo & Taylor, 1976). (b) A plot of $Na_2O + K_2O$ – CaO vs SiO_2 (wt %) (Frost *et al.* 2001). (c) A plot of A/CNK (molar $Al_2O_3/(CaO + Na_2O + K_2O)$) vs A/NK (molar $Al_2O_3/(Na_2O + K_2O)$) (Shand, 1948). (d) A plot of $FeO_{total}/(FeO_{total} + MgO)$ vs SiO_2 (wt %) (Frost *et al.* 2001). All oxides are calculated as anhydrous. Data sources for the compiled Eocene–Oligocene EIMB igneous rocks are listed in Figure 8.

Material Table S4). Comparing the elemental ratios in rocks of this study with mantle- or crustal-derived melts emphasizes that these magmatic rocks have elemental ratios that fall between these two end-members, and the evolved magmas could be generated during mantle–crust assimilation. Additionally, significant positive anomalies in Pb and K can be related to the assimilation of crustal materials during magma ascent (see Fig. 11b, d; Taylor & McLennan, 1985).

We emphasize that the assimilation of continental crust during magma ascent to the surface can affect the isotopic signatures of the magma (e.g. high Sr and low Nd isotopic ratios). On the isotopic $^{87}Sr/^{86}Sr_{(i)}$ and $^{143}Nd/^{144}Nd_{(i)}$ diagram (Fig. 13a), we consider a near-primitive basaltic lava of the Eocene–Oligocene EIMB as representative of juvenile mantle-derived melt (starting melt). In this plot, the Eocene–Oligocene EIMB magmatic rocks have a mixed origin. The mantle-derived melt is a significant component, and the continental crust (Cadomian upper crust) is a minor one. The isotopic mixing model suggests that the EIMB magmas formed by more than ~90 % juvenile mantle-derived melt and less than ~10 % Cadomian continental crust by assimilation-fractional crystallization (AFC) processes during magma ascent. In this respect, the Eocene–Oligocene EIMB magmatic rocks show increasing Th/La and $^{87}Sr/^{86}Sr_{(i)}$ and decreasing $\epsilon Nd_{(i)}$ values along with increasing SiO_2, attesting to AFC processes during EIMB magmatic evolution (Fig. 13b–d). Our EIMB magmatic samples also record evidence of AFC during ascent and stagnation in the continental crust by the presence of some inherited zircons with $^{238}U/^{206}Pb$ ages of 440 Ma to 60 Ma. Therefore, the wide isotopic variations of the Eocene–Oligocene EIMB magmatic rocks can be explained by different amounts of crustal contamination during magma ascent.

Based on the presented geochemical data, mantle wedge had a significant role in forming the EIMB parental melts. In the following, we will discuss that the parental magmas were generated from a sub-continental lithospheric mantle (SCLM) or asthenospheric mantle. Although there are no primitive or near-primitive magmatic rocks in our analysed samples (online Supplementary Material Table S4), in our compiled dataset ($n = 108$) three basaltic

https://doi.org/10.1017/S0016756822001066 Published online by Cambridge University Press

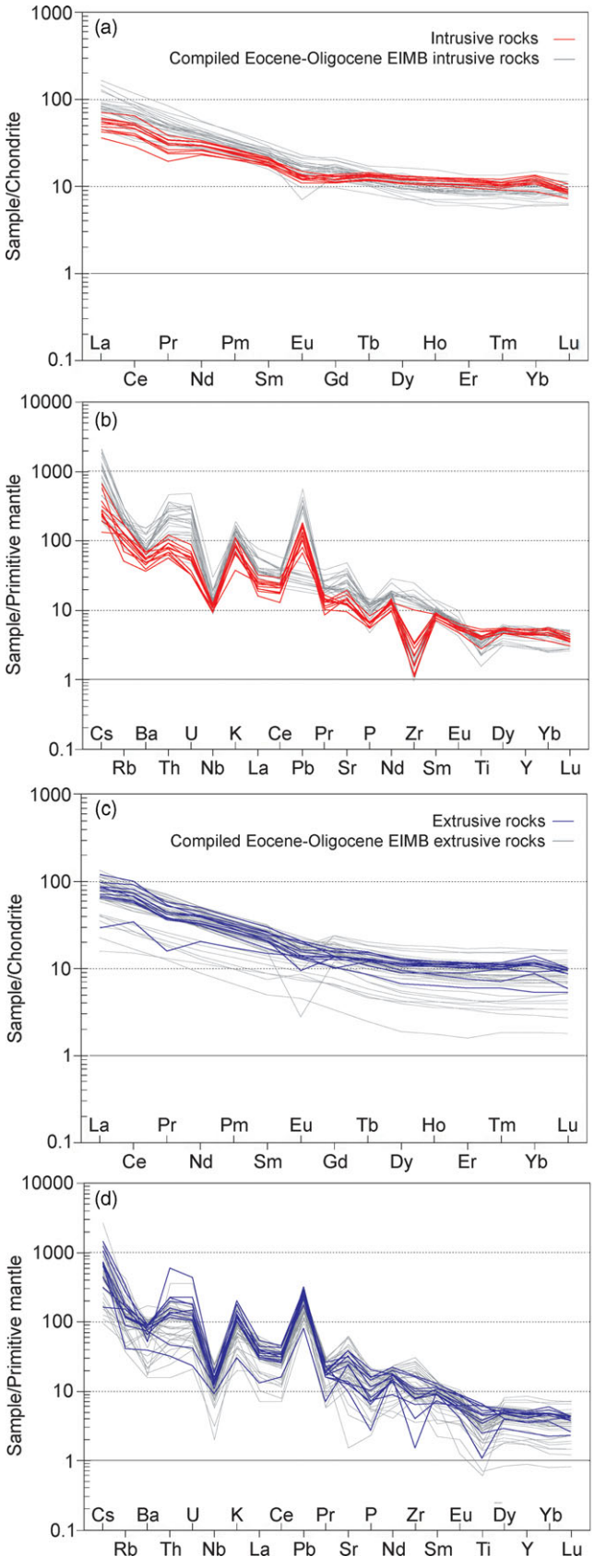


Fig. 11. (Colour online) Chondrite-normalized REE and primitive-mantle-normalized multi-element diagrams for the EIMB magmatic rocks. Normalizing values for chondrite and primitive mantle are taken from Boynton (1984) and Sun and McDonough (1989). Data sources for the compiled Eocene–Oligocene EIMB igneous rocks are listed in Figure 8.

rocks (samples 07-50, 08-Z-11 and 10-09; Pang *et al.* 2013) show near-primitive magmatic characteristics (e.g. SiO_2 = 48.97–50.57 (wt %), MgO = 11.64–13.45 (wt %), Mg# = 72.2–76, Cr = 438–1067 ppm and Ni = 299–556 ppm). The Nb/La ratio could help discriminate lithospheric from asthenospheric mantle sources (Abdel-Rahman & Nassar, 2004; Morata *et al.* 2005). The low Nb/La ratios of 0.33 to 0.42 from the near-primitive EIMB magmatic rocks indicate a SCLM source consistent with radiogenic Nd isotopic values ($\epsilon Nd_{(i)}$ = 3–3.6) for these rocks. Moreover, deep asthenospheric mantle-derived melts are characterized by strong enrichment in LREEs relative to HREEs similar to OIB-like melts. In contrast, the REEs and trace element patterns of the Eocene–Oligocene EIMB magmatic rocks are not consistent with a deep asthenospheric mantle source (see Fig. 11).

Consequently, based on all elemental and isotopic ratios, we consider that the near-primary basaltic lavas from the Eocene–Oligocene EIMB could have originated from a subduction-modified SCLM. A metasomatized SCLM source has previously been proposed for the genesis of Eocene–Oligocene magmatic rocks from NW, N and NE Iran (e.g. Verdel *et al.* 2011; Sepidbar *et al.* 2019; Shafaii Moghadam *et al.* 2020). The parental melts are further fractionated and contaminated with an upper continental crust of eastern Iran during ascent and stagnation at a shallow depth to produce the Eocene–Oligocene EIMB evolved melts. The $La_{(N)}/Yb_{(N)}$ ratios of the Eocene–Oligocene EIMB igneous rocks range from 2.53 to 16.55 (online Supplementary Material Table S4 and compiled data), which are lower than those for a garnet-bearing mantle source ($La_{(N)}/Yb_{(N)} > 20$; Martin, 1987). Also, the Sm/Yb ratios of the EIMB magmatic samples range from 1.2 to 3.8 (online Supplementary Material Table S4 and compiled data), highlighting that the magmatic rocks probably formed within spinel–lherzolite stability fields (Kay, 2001), suggesting their formation at depths less than 75 km.

6.b. Tectono-magmatic implication for the Eocene–Oligocene EIMB magmatic rocks

Three scenarios have been proposed to explain the origin of the voluminous Eocene–Oligocene igneous rocks within the EIMB. In the first scenario, Verdel *et al.* (2011) suggested that the Eocene–Oligocene magmatism of the EIMB, as in the UDMB and AAMB, was related to an extensional tectonic environment that prevailed in the Iranian Plateau, overlying the subducting Neo-Tethyan oceanic lithosphere. In this model, roll-back of the subducting slab caused lithospheric thinning and extension of the overriding plate (the Iranian Plateau), leading to the decompression melting of metasomatized lithospheric mantle and the formation of elongated rift basins. In the second scenario, Pang *et al.* (2013) suggested that westward subduction of the Sistan oceanic lithosphere followed by the collision between the Lut and Afghan blocks formed a thickened continental lithosphere in the Late Cretaceous – Palaeocene; this thickened lithospheric root subsequently collapsed, triggering asthenospheric upwelling and magmatism in an extensional post-collisional setting during the Eocene to Oligocene. In the third scenario, the Eocene–Oligocene EIMB magmatic rocks were attributed to an Andean-type active continental margin setting. In this model, igneous rocks of the Lut block resulted from westward subduction of the Sistan oceanic lithosphere beneath the Lut block during the Cretaceous to Palaeogene (e.g. Arjmandzadeh *et al.* 2011; Beydokhti *et al.* 2015; Samiee *et al.* 2016; Nadermezerji *et al.* 2018).

https://doi.org/10.1017/S0016756822001066 Published online by Cambridge University Press

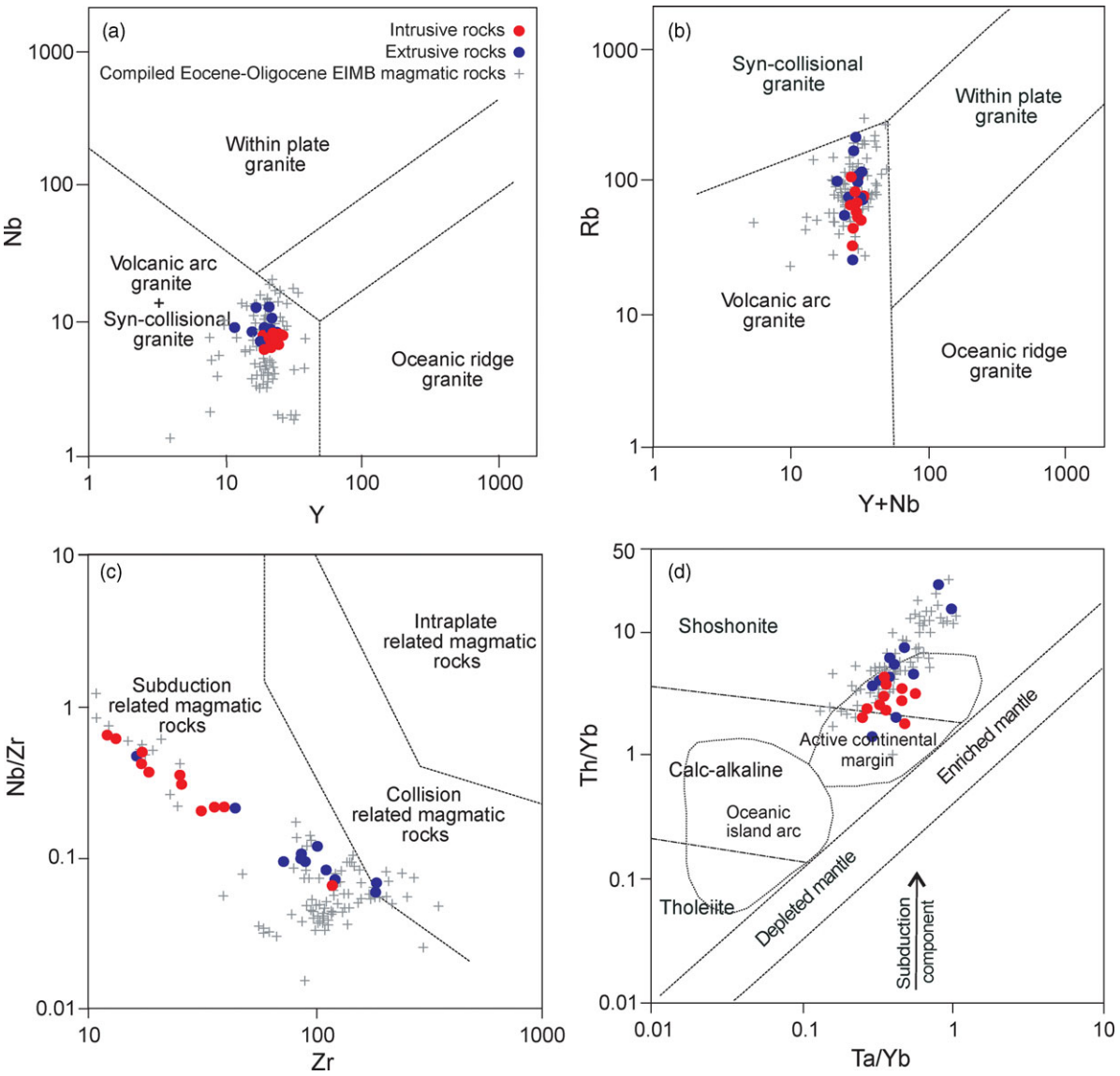


Fig. 12. (Colour online) Tectonomagmatic discrimination diagrams for the EIMB magmatic rocks. (a) Correlation of Nb vs Y (Pearce *et al.* 1984). (b) Correlation of Rb vs Y + Nb (Pearce *et al.* 1984). (c) Correlation of Nb/Zr vs Zr (Thieblemont & Tegyey, 1994). (d) Correlation of Th/Yb vs Ta/Yb (Pearce, 1982). Data sources for the compiled Eocene–Oligocene EIMB igneous rocks are listed in Figure 8.

Generally, the geochemical and isotopic results (including our new and compiled data) indicate that metasomatized SCLM is the primary mantle source for the Eocene–Oligocene EIMB magmatic rocks. One of the outstanding questions is, did the subduction-related components come from the westward subduction of the Sistan oceanic lithosphere beneath the Lut block or the northeastward subduction of the Neo-Tethyan oceanic lithosphere underneath the Iranian Plateau (including EIMB region)? Based on geochemical investigations, some studies proposed that the subduction-related characteristics of the EIMB magmatic rocks could be inherited by the westward subduction of the Sistan oceanic lithosphere beneath the Lut block during the pre-Late Cretaceous along the so-called Sistan suture zone (e.g. Arjmandzadeh *et al.* 2011; Pang *et al.* 2013; Beydokhti *et al.* 2015; Samiee *et al.* 2016; Nadermezerji *et al.* 2018; Sepidbar *et al.* 2018). On the other hand, structural evidence revealed that the accretionary wedge of the Sistan suture zone is generated due to the eastward subduction of the Sistan Ocean beneath the Afghan block (Fotoohi Rad *et al.* 2005; Angiboust *et al.* 2013; Bonnet *et al.* 2018). Jentzer *et al.* (2020) believed that the Late Cretaceous subduction-related magmatism in the west of the Afghan block was formed due to the NE-dipping subduction of the Sistan oceanic lithosphere beneath the stretched margin of the Afghan block. In any case, the subduction of the Sistan oceanic lithosphere beneath the Afghan block could not supply the subduction components into the mantle beneath the EIMB. We believe that the subduction-related characteristic of the EIMB magmatic rocks is more likely controlled by subduction processes along the Zagros suture zone. A unique NE-dipping subducting oceanic crust beneath the Iranian Plateau is also supported by seismic survey and mantle tomography (e.g. Al-Lazki *et al.* 2004; Molinaro *et al.* 2005; Authemayou *et al.* 2006; Shomali *et al.* 2011;

https://doi.org/10.1017/S0016756822001066 Published online by Cambridge University Press

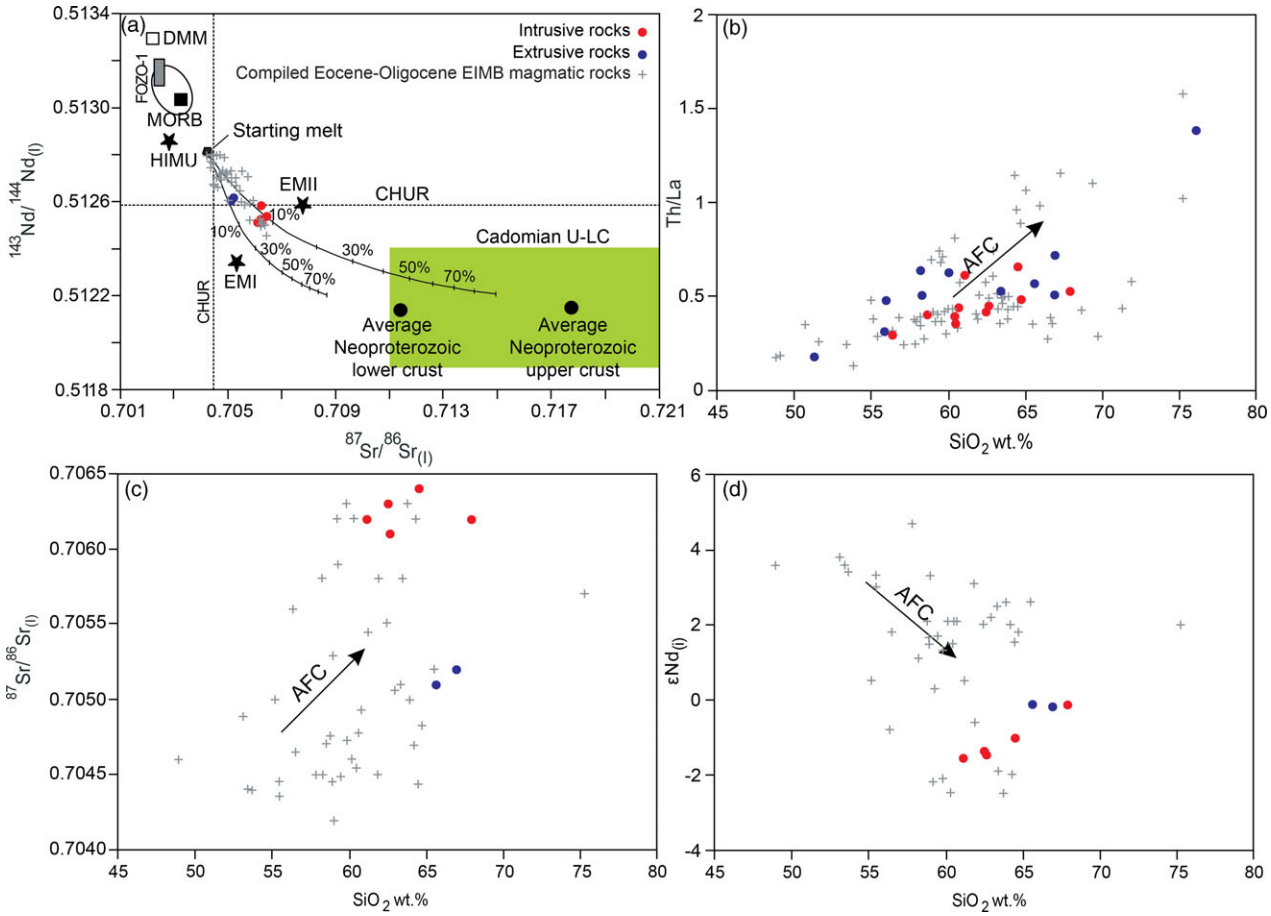


Fig. 13. (Colour online) Isotopic and compositional diagrams for the EIMB magmatic rocks. (a) Relationship of $^{143}Nd/^{144}Nd_{(i)}$ vs $^{87}Sr/^{86}Sr_{(i)}$. (b) Relationship of Th/La vs SiO_2 (wt %). (c) Relationship of $^{87}Sr/^{86}Sr_{(i)}$ vs SiO_2 (wt %). (d) Relationship of $\epsilon Nd_{(i)}$ vs SiO_2 (wt %). The SiO_2 is calculated as anhydrous. Data sources for the compiled Eocene–Oligocene EIMB igneous rocks are listed in Figure 8. Compositional domains for mantle components (HIMU, EMI, EMII and DMM) are taken from Zindler and Hart (1986). The data source for FOZO-1 is taken from Hart *et al.* (1992). CHUR: chondritic uniform reservoir. The composition of the starting melt, a near-primitive basalt sample 07-50 (SiO_2 = 48.97 (wt %); MgO = 11.77 (wt %); Mg# = 72.6; Cr = 520 ppm; Ni = 299 ppm; $^{87}Sr/^{86}Sr_{(i)}$ = 0.7044; and $^{143}Nd/^{144}Nd_{(i)}$ = 0.5128), is adopted from Pang *et al.* (2013). The assimilation-fractional crystallization (AFC) trends are simulated based on the algorithm proposed by Ersoy (2013). Iran's Neoproterozoic upper and lower continental crust (Cadomian U-LC) is taken from Shafaii Moghadam *et al.* (2015*a*).

Entezar-Saadat *et al.* 2017). A similar mechanism has also been suggested for the Eocene–Oligocene magmatism in the UDMB, AAMB and NEIMB (e.g. Verdel *et al.* 2011; Sepidbar *et al.* 2019; Shafaii Moghadam *et al.* 2020).

A geodynamic model for Eocene–Oligocene EIMB magmatism should be able to explain how: (i) subduction-related metasomatism underneath the EIMB was formed by northeastward subduction of the Neo-Tethyan oceanic lithosphere beneath the Iranian Plateau; (ii) near-primitive mafic rocks of the EIMB were derived from a metasomatized SCLM and not necessarily from a depleted MORB mantle (DMM) or a deep asthenospheric mantle source (e.g. HIMU-, FOZO- and OIB-like); and (iii) the evolved intermediate to felsic igneous rocks show contamination with continental crust.

We propose that the voluminous Eocene–Oligocene EIMB subduction-related magmatic rocks were generated in an extensional tectonic context accompanied by lithospheric thinning in an overlying plate (Fig. 14). These rocks are similar to the other extensional subduction-related magmatic flare-ups (e.g. UDMB, AAMB and NEIMB), which were simultaneously formed within the Iranian Plateau. The extensional tectonic regime within the Iranian Plateau during the Palaeogene time (especially Eocene–Oligocene) is supported by the abundant metamorphic core complex formation and the presence of shallow to deep marine sediments interbedded with high-volume volcanic rocks (Berberian & King. 1981; Brunet *et al.* 2003; Vincent *et al.* 2005; Ballato *et al.* 2011; Verdel *et al.* 2011). Numerous Eocene–Oligocene volcano-sedimentary strata indicate a shallow submarine extensional basin within the EIMB. Moreover, the presence of pillow lava structure in some lithological units within the EIMB (~100 km west of the Zahedan; Camp & Griffis, 1982) could be attributed to the eruption in a water-filled extensional basin. The extensional environment and its associated high-volume magmatic rocks within the Iranian Plateau are likely related to the steepening of old Neo-Tethyan oceanic slab beneath the Iranian Plateau, leading to trench roll-back (for more details, see Verdel *et al.* 2011; Shafaii Moghadam *et al.* 2018, 2020; Sepidbar *et al.* 2019).

In our scenario for the formation of EIMB magmatic rocks, similar to what has been proposed for the UDMB, AAMB and NEIMB magmatic flare-ups (Verdel *et al.* 2011; Sepidbar *et al.*

https://doi.org/10.1017/S0016756822001066 Published online by Cambridge University Press

Table 1. Available geochronological and geochemical data for the Eocene–Oligocene EIMB magmatic rocks

EIMB magmatism	Long./Lat.	Ages (methods)	Rock types	Geochemical characteristics	Tectono-magmatic settings	References
Chah-Shaljami intrusion	52° 57′ 31″ to 52° 59′ 25″ E 31° 45′ 36″ to 31° 45′ 50″ N	33.5 ± 1 Ma (^{40}Ar–^{39}Ar)	Diorite/granodiorite/quartz–monzonite	These intrusive rocks belong to I-type granitoids and have high-K calc-alkaline to shoshonitic affinities. REE and trace element patterns display LREE/HREE enrichment, LILE enrichment (Rb, Ba and Cs) and HFSE depletion (Nb, Ti and Y). $^{87}Sr/^{86}Sr_{(i)} = 0.7047$ to 0.7051. $^{143}Nd/^{144}Nd_{(i)} = 0.51264$ to 0.51276. $\epsilon Nd_{(i)} = +1.9$ to $+2.7$. Elemental and isotopic data indicate that parental magmas were generated from a subduction-modified mantle wedge.	Active continental margin Westward subduction of Sistan oceanic lithosphere beneath the Lut block	Arjmandzadeh *et al.* (2011)
Mahoor intrusion	58° 51′ 30″ to 58° 56′ 0″ E 31° 06′ 00″ to 31° 13′ 00″ N	31.9 ± 0.2 Ma (U–Pb)	Gabbrodiorite/diorite/monzodiorite/tonalite	These intrusive rocks belong to I-type granitoids and have calc-alkaline to high-K calc-alkaline affinities. REE and trace element patterns display LREE/HREE enrichment, LILE enrichment and HFSE depletion (Ta, Nb and Ti). $^{87}Sr/^{86}Sr_{(i)} = 0.7055$ to 0.7063. $^{143}Nd/^{144}Nd_{(i)} = 0.51245$ to 0.51259. $\epsilon Nd_{(i)} = -0.6$ to -2.5. Elemental and isotopic data are in good agreement with the formation of this intrusion above a subduction zone. Both magma differentiation and crustal contamination occurred during magma ascent to crustal levels.	Active continental margin Westward subduction of Sistan oceanic lithosphere beneath the Lut block	Beydokhti *et al.* (2015)
Khunik intrusion	59° 09′ 00″ to 59° 12′ 00″ E 32° 21′ 00″ to 32° 25′ 00″ N	38 ± 1 Ma (U–Pb)	Diorite/monzodiorite/quartz–monzodiorite/quartz–monzonite	These intrusive rocks belong to I-type granitoids and have high-K calc-alkaline to shoshonitic affinities. REE and trace element patterns display LREEs/HREE enrichment, LILE enrichment (Rb, Ba and Cs) and HFSE depletion. $^{87}Sr/^{86}Sr_{(i)} = 0.7042$ to 0.7048. $^{143}Nd/^{144}Nd_{(i)} = 0.51269$ to 0.51279. $\epsilon Nd_{(i)} = +1.5$ to $+2.5$. According to elemental and isotopic data, parental magmas were generated from a subduction-related mantle wedge and crustal contamination had a minor role during magmatic evolution.	Active continental margin Westward subduction of Sistan oceanic lithosphere beneath the Lut block	Samiee *et al.* (2016)
Shah-Soltan Ali intrusion	58° 57′ 10″ to 58° 59′ 40″ E 32° 26′ 00″ to 32° 29′ 50″ N	38.3 ± 0.5 Ma (U–Pb)	Diorite/monzodiorite/monzonite	These intrusive rocks belong to I-type granitoids and have high-K calc-alkaline to shoshonitic affinities. REE and trace element patterns display LREE/HREE enrichment, LILE enrichment and HFSE depletion (Nb, Ti and Zr). $^{87}Sr/^{86}Sr_{(i)} = 0.7043$ to 0.7052. $^{143}Nd/^{144}Nd_{(i)} = 0.51267$ to 0.51278. $\epsilon Nd_{(i)} = +1.48$ to $+3.82$. Isotopic and elemental data	Active continental margin Westward subduction of Sistan oceanic lithosphere beneath the Lut block	Nadermezerji *et al.* (2018)

(*Continued*)

https://doi.org/10.1017/S0016756822001066 Published online by Cambridge University Press

Table 1. (*Continued*)

EIMB magmatism	Long./Lat.	Ages (methods)	Rock types	Geochemical characteristics	Tectono-magmatic settings	References
				indicate that parental magmas were derived from a metasomatized mantle source. Parental magmas were contaminated with crustal material during ascent.		
Koudakan intrusion	58° 57′ 00″ to 59° 02′ 00″ E 31° 56′ 00″ to 31° 59′ 00″ N	37.9 ± 0.8 Ma to 41.7 ± 3.4 Ma (U–Pb)	Monzonite/quartz–monzonite/granite	These intrusive rocks belong to I-type granitoids and have high-K calc-alkaline to shoshonitic affinities. REE and trace element patterns display LREE/HREE enrichment, LILE enrichment (K, Rb and Cs), Th, U and Pb enrichment and HFSE depletion (Nb, Zr and Ti). $^{87}Sr/^{86}Sr_{(i)} = 0.7044$ to 0.7047. $^{143}Nd/^{144}Nd_{(i)} = 0.51266–0.51267$. $\epsilon Nd_{(i)} = +1.32$ to $+1.68$. Elemental and isotopic data reveal a metasomatized subcontinental lithospheric mantle source and different amounts of crustal contamination.	Post-collisional setting Subduction-related signature is inherited by northeastward subduction of Neo-Tethyan oceanic lithosphere beneath the Iranian Plateau.	Omidianfar *et al.* (2020)
EIMB volcanic rocks	57° 45′ 00″ to 60° 45′ 00″ E 31° 00′ 0″ to 34° 00′ 00″ N	~46 Ma to ~25 Ma ($^{40}Ar–^{39}Ar$)	Basalt/rhyolite/pyroclastic rocks	These magmatic rocks have calc-alkaline to shoshonitic affinities. REE and trace element patterns display LILE enrichment, Th and Pb enrichment and HFSE depletion (Nb, Ta and Ti). $^{87}Sr/^{86}Sr_{(i)} = 0.7042$ to 0.7065. $^{143}Nd/^{144}Nd_{(i)} = 0.51250$ to 0.51290. $\epsilon Nd_{(i)} = -4.9$ to $+5.5$. Elemental and isotopic data indicate that parental magmas were derived from partial melting of subduction-modified mantle wedge. The parental magmas were contaminated with crustal material during ascent.	Post-collisional setting Subduction-related signature is inherited by westward subduction of the Sistan oceanic lithosphere beneath the Lut block.	Pang *et al.* (2013)
Sangan Magmatic Complex	60° 10′ 00″ to 60° 55′ 00″ E 34° 15′ 00″ to 35° 00′ 00″ N	~44 Ma to ~40 Ma (U–Pb)	Dacite/trachydacite/trachyte/pyroclastic rocks/granite/syenogranite	These magmatic rocks have typical high-K calc-alkaline to shoshonitic affinities. REE and trace element patterns display LILE enrichment and HFSE depletion. $^{87}Sr/^{86}Sr_{(i)} = 0.7034$ to 0.7116. $^{143}Nd/^{144}Nd_{(i)} = 0.51246$ to 0.51274. $\epsilon Nd_{(i)} = -5.3$ to $+0.7$. Elemental and isotopic data suggest that parental magmas were generated by the interaction of mantle-derived melts with continental crust through AFC processes.	Post-collisional setting	Sepidbar *et al.* (2018)

2019; Shafaii Moghadam *et al.* 2020), relatively steep-angle subduction of the Neo-Tethyan oceanic lithosphere beneath the Iranian Plateau occurred during the Cretaceous. It was followed by flat-slab subduction, leading to the addition of slab-derived fluids/melts into the SCLM under the EIMB. At a later stage, during the Eocene to Oligocene, slab roll-back of the Neo-Tethyan oceanic lithosphere and subsequent asthenospheric upwelling into the mantle wedge led to lithospheric thinning, partial melting of metasomatized SCLM and the generation of EIMB extensional subduction-related magmatism (Fig. 14). The SCLM-derived melts then interacted with the continental crust during magma ascent (AFC process).

https://doi.org/10.1017/S0016756822001066 Published online by Cambridge University Press

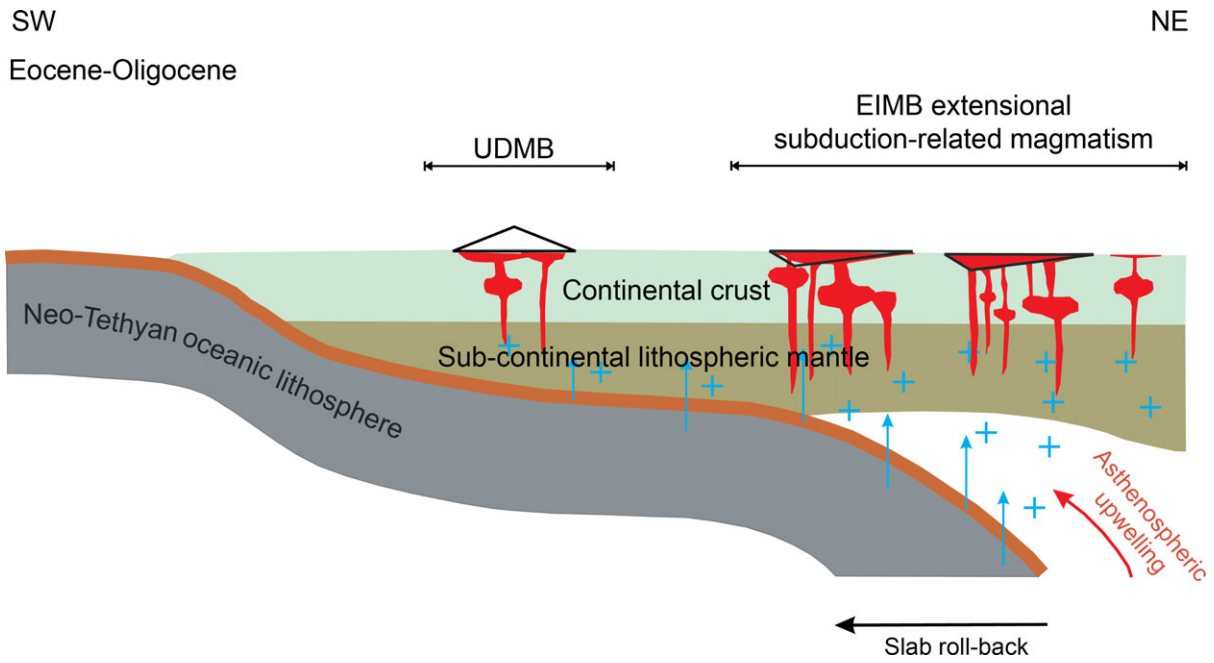


Fig. 14. (Colour online) A geodynamic model proposes the formation of the EIMB magmatic rocks. The EIMB magmatism is assumed to be formed during the Eocene–Oligocene due to the Neo-Tethys slab roll-back, asthenospheric upwelling and lithospheric extension.

7. Conclusions

Our new zircon U–Pb data from igneous rocks of the region south of Birjand yielded ages of 43.6 ± 0.4 Ma to 39.5 ± 0.6 Ma, consistent with those reported from other EIMB magmatic rocks (~46 Ma to ~25 Ma). The Eocene–Oligocene EIMB igneous rocks are represented by slight to moderate LREE/HREE enrichment (e.g. $La_N/Yb_N = 2.5$ to 16.6), positive Cs, Rb, Ba, K, Th and U anomalies, and negative Nb, Zr and Ti anomalies, which attest to their derivation in a subduction-related environment. The geochemical and isotopic data show that the magmatic rocks are co-genetic and that their parental magmas were derived from a metasomatized SCLM source. Furthermore, the Sr–Nd isotopic ratios reveal an interaction of parental melts with small amounts (<10 %) of Iran's Cadomian upper continental crust during ascent. We propose that Eocene–Oligocene magmatism in eastern Iran was formed in an extensional subduction-related tectonic environment. In this formwork, slab roll-back accompanied by asthenospheric upwelling triggered lithospheric thinning, partially melting metasomatized SCLM and generation of EIMB primary magmas.

Supplementary material. To view supplementary material for this article, please visit https://doi.org/10.1017/S0016756822001066

Acknowledgements. This research received no specific grant from any commercial or not-for-profit funding agency. The authors are greatly indebted to Dr Sarah Sherlock, editor of the *Geological Magazine*, Dr Scott A. Whattam, Dr Michael Bröcker and two anonymous reviewers for constructive discussions, thorough revisions and valuable comments concerning the manuscript.

Conflict of interest. None.

References

Abdel-Rahman AFM and Nassar PE (2004) Cenozoic volcanism in the Middle East: petrogenesis of alkali basalts from northern Lebanon. *Geological Magazine* **141**, 545–63.

Agard P, Omrani J, Jolivet L, Whitechurch H, Vrielynck B, Spakman W, Monié P, Meyer B and Wortel R (2011) Zagros orogeny: a subduction-dominated process. *Geological Magazine* **148**, 692–725.

Al-Lazki AI, Sandvol E, Seber D, Barazangi M, Turkelli N and Mohamad R (2004) Pn tomographic imaging of mantle lid velocity and anisotropy at the junction of the Arabian, Eurasian and African plates. *Geophysical Journal International* **158**, 1024–40.

Angiboust S, Agard P, De Hoog JCM, Omrani J and Plunder A (2013) Insights on deep, accretionary subduction processes from the Sistan ophiolitic 'mélange' (Eastern Iran). *Lithos* **156–159**, 139–58.

Annen C, Blundy JD and Sparks RSJ (2006) The genesis of intermediate and silicic magmas in deep crustal hot zones. *Journal of Petrology* **47**, 505–39.

Arjmandzadeh R, Karimpour MH, Mazaheri SA, Santos JF, Medina JM and Homam SM (2011) Sr-Nd isotope geochemistry and petrogenesis of the Chah-Shaljami granitoids (Lut Block, Eastern Iran). *Journal of Asian Earth Sciences* **41**, 283–96.

Authemayou C, Chardon D, Bellier O, Malekzadeh Z, Shabanian E and Abbassi MR (2006) Late Cenozoic partitioning of oblique plate convergence in the Zagros fold-and-thrust belt (Iran). *Tectonics* **25**, TC3002. doi: 10.1029/2005TC001860.

Avanzinelli R, Lustrino M, Mattei M, Melluso L and Conticelli S (2009) Potassic and ultrapotassic magmatism in the circum-Tyrrhenian region: significance of carbonated pelitic vs. pelitic sediment recycling at destructive plate margins. *Lithos* **113**, 213–27.

Babazadeh SA and De Wever P (2004) Radiolarian Cretaceous age of Soulabest radiolarites in ophiolite suite of eastern Iran. *Bulletin de la Société Géologique de France* **175**, 121–9.

Ballato P, Uba CE, Landgrfa A, Strecker MR, Sudo M, Stockli DF, Friedrih A and Tabatabaei SH (2011) Arabia-Eurasia continental collision: insights from late Tertiary foreland-basin evolution in the Alborz Mountains, northern Iran. *Geological. Society of America Bulletin* **123**, 106–31.

Bayet-Gol A, Monaco P, Jalili F and Mahmuudy-Gharaie MH (2016) Depositional environments and ichnology of Upper Cretaceous deep-marine deposits in the Sistan Suture Zone, Birjand, Eastern Iran. *Cretaceous Research* **60**, 28–51.

Berberian M (2014) Active tectonics and geologic setting of the Iranian Plateau. *Developments in Earth Surface Processes* **17**, 151–71.

Berberian M and King GCP (1981) Towards a paleogeography and tectonic evolution of Iran. *Canadian Journal of Earth Sciences* **18**, 210–65.

https://doi.org/10.1017/S0016756822001066 Published online by Cambridge University Press

Beydokhti RM, Karimpour MH, Mazaheri SA, Santos JF and Klötzli U (2015) U-Pb zircon geochronology, Sr-Nd geochemistry, petrogenesis and tectonic setting of Mahoor granitoid rocks (Lut Block, Eastern Iran). *Journal of Asian Earth Sciences* **111**, 192–205.

Bonnet G, Agard P, Angiboust S, Monié P, Jentzer M, Omrani J, Whitechurch H and Fournier M (2018) Tectonic slicing and mixing processes along the subduction interface: the Sistan example (Eastern Iran). *Lithos* **310–311**, 269–87.

Boynton WV (1984) Cosmochemistry of the rare earth elements: meteorite studies. *Developments in Geochemistry* **2**, 63–114.

Bröcker M, Fotoohi Rad G, Burgess R, Theunissen S, Paderin I, Rodionov N and Salimi Z (2013) New age constraints for the geodynamic evolution of the Sistan Suture Zone, eastern Iran. *Lithos* **170–171**, 17–34.

Bröcker M, Hövelkröger Y, Fotoohi Rad G, Berndt J, Scherer EE, Kurzawa T and Moslempour ME (2022) The magmatic and tectono-metamorphic history of the Sistan suture zone, Iran: new insights into a key region for the convergence between the Lut and Afghan blocks. *Journal of Asian Earth Sciences* **236**, 105313.

Brunet MF, Korotaev MV, Ershow AV and Nikishin AM (2003) The South Caspian Basin: a review of its evolution from subsidence modelling. *Sedimentary Geology* **156**, 119–48.

Camp VE and Griffis RJ (1982) Character, genesis and tectonic setting of igneous rocks in the Sistan suture zone, eastern Iran. *Lithos* **15**, 221–39.

Chappell BW and White AJR (2001) Two contrasting granite types: 25 years later. *Australian Journal of Earth Sciences* **48**, 489–99.

Chiu H-Y, Chung S-L, Zarrinkoub MH, Mohammadi SS, Khatib MM and Iizuka Y (2013) Zircon U–Pb age constraints from Iran on the magmatic evolution related to Neotethyan subduction and Zagros orogeny. *Lithos* **162**, 70–87.

Corfu F, Hanchar JM, Hoskin PWO and Kinny P (2003) Atlas of zircon textures. *Reviews in Mineralogy and Geochemistry* **53**, 469–500.

Eby GN (1992) Chemical subdivision of the A-type granitoids: petrogenetic and tectonic implications. *Geology* **20**, 641–4.

Emami MH, Mir Mohammad Sadeghi M and Omrani SJ (1993) *Magmatic Map of Iran, scale 1:1000000.* Tehran: Geological Survey of Iran.

Entezar-Saadat V, Motavally-Anbaran SH and Zeyen H (2017) Lithospheric structure of the eastern Iranian plateau from integrated geophysical modeling: a transect from Makran to the Turan platform. *Journal of Asian Earth Sciences* **138**, 357–66.

Ersoy EY (2013) PETROMODELER (Petrological Modeler): a Microsoft (R) Excel (R) spreadsheet program for modelling melting, mixing, crystallization and assimilation processes in magmatic systems. *Turkish Journal of Earth Sciences* **22**, 115–25.

Fotoohi Rad GR, Droop GTR, Amini S and Moazzen M (2005) Eclogites and blueschists of the Sistan Suture Zone, eastern Iran: a comparison of P-T histories from a subduction mélange. *Lithos* **84**, 1–24.

Frost BR, Barnes CG, Collins WJ, Arculus RJ, Ellis DJ and Frost CD (2001) A geochemical classification for granitic rocks. *Journal of Petrology* **42**, 2033–48.

Green TH (1995) Significance of Nb/Ta as an indicator of geochemical processes in the crust-mantle system. *Chemical Geology* **120**, 347–59.

Hart SR, Hauri EH, Oschmann LA and Whitehead JA (1992) Mantle plumes and entrainment: isotopic evidence. *Science* **256**, 517–20.

Hassanzadeh J and Wernicke BP (2016) The Neotethyan Sanandaj-Sirjan zone of Iran as an archetype for passive margin-arc transitions. *Tectonics* **35**, 586–621.

Hempton MR (1978) Constraints on Arabian plate motion and extensional history of the Red Sea. *Tectonics* **6**, 687–705.

Henderson P (1983) *Rare Earth Element Geochemistry*. Amsterdam: Elsevier, 510 pp.

Hoskin PWO (1998) Minor and trace element analysis of natural zircon ($ZrSiO_4$) by SIMS and laser ablation ICPMS: a consideration and comparison of two broadly competitive techniques. *Journal of Trace and Microprobe Techniques* **16**, 301–26.

Hou ZQ, Gao YF, Qu XM, Rui ZY and Mo XX (2004) Origin of adakitic intrusives generated during mid-Miocene east-west extension in southern Tibet. *Earth and Planetary Science Letters* **220**, 139–55.

Jentzer M, Whitechurch H, Agard P, Ulrich M, Caron B, Zarrinkoub MH, Kohansal R, Miguet L, Omrani J and Fournier M (2020) Late Cretaceous calc-alkaline and adakitic magmatism in the Sistan suture zone (Eastern Iran): implications for subduction polarity and regional tectonics. *Journal of Asian Earth Sciences* **204**, 104588.

Kay SM (2001) Central Andean ore deposits linked to evolving shallow subduction systems and thickening crust. *GSA Today* **11**, 4–9.

Kerr PF (1959) *Optical Mineralogy*, 3rd edn. New York: McGraw-Hill Book Co., Inc., 442 pp.

Khodaverdian A, Zafarani H and Rahimian M (2015) Long term fault slip rates, distributed deformation rates and forecast of seismicity in the Iranian Plateau. *Tectonics* **34**, 2190–220.

Mamani M, Wörner G and Thouret J (2008) Tracing a major crustal domain boundary based on geochemistry of minor volcanic centres in southern Peru. In *7th International Symposium on Andean Geodynamics*, Paris, Institut de recherché pour le développement and Université Nice Sophia Antipolis, 298–301.

Martin H (1987) Petrogenesis of archaean trondhjemites, tonalites, and granodiorites from Eastern Finland: major and trace element geochemistry. *Journal of Petrology* **28**, 921–53.

Middlemost EAK (1994) Naming materials in the magma/igneous rock system. *Earth Science Reviews* **37**, 215–24.

Molinaro M, Zeyen H and Laurencin X (2005) Lithospheric structure beneath the south-eastern Zagros Mountains, Iran: recent slab break-off? *Terra Nova* **17**, 1–6.

Monsef I, Monsef R, Mata J, Zhang Z, Pirouz M, Rezaeian M, Esmaeili R and Xiao W (2018) Evidence for an early-MORB to fore-arc evolution within the Zagros suture zone: constraints from zircon U-Pb geochronology and geochemistry of the Neyriz ophiolite (South Iran). *Gondwana Research* **62**, 287–305.

Monsef R, Monsef I and Rahgoshay M (2014) Geodynamic significance of the Janatabad peridotites and associated chromitites (S Iran): implications for subduction initiation. *Ofioliti* **39**, 67–78.

Monsef I, Rahgoshay M, Mohajel M and Moghadam HS (2010) Peridotites from the Khoy Ophiolitic Complex, NW Iran: evidence of mantle dynamics in a supra-subduction-zone context. *Journal of Asian Earth Sciences* **38**, 105–20.

Monsef I, Zhang Z, Shabanian E, Le Roux P and Rahgoshay M (2022) Tethyan subduction and Cretaceous rift magmatism at the southern margin of Eurasia: evidence for crustal evolution of the South Caspian Basin. *Earth-Science Reviews* **228**, 104012. doi: 10.1016/j.earscirev.2022.104012.

Morata D, Oliva C, de la Cruz R and Suárez M (2005) The Bandurrias gabbro: Late Oligocene alkaline magmatism in the Patagonian Cordillera. *Journal of South American Earth Sciences* **18**, 147–62.

Nadermezerji S, Karimpour MH, Malekzadeh Shafaroudi A, Francisco Santos J, Mathur R and Ribeiro S (2018) U–Pb geochronology, Sr–Nd isotopic compositions, geochemistry and petrogenesis of Shah Soltan Ali granitoids, Birjand, Eastern Iran. *Chemie der Erde* **78**, 299–313.

Omidianfar S, Monsef I, Rahgoshay M, Zheng J and Cousens B (2020) The middle Eocene high-K magmatism in Eastern Iran Magmatic Belt: constraints from U-Pb zircon geochronology and Sr-Nd isotopic ratios. *International Geology Review* **62**, 1751–68.

Omrani J, Agard P, Whitechurch H, Benoit M, Prouteau G and Jolivet L (2008) Arc-magmatism and subduction history beneath the Zagros Mountains, Iran: a new report of adakites and geodynamic consequences. *Lithos* **106**, 380–98.

Paknia M, Ballato P, Heidarzadeh G, Cifelli F, Hassanzadeh J, Vezzoli G, Mirzaie Ataabadi M, Ghassemi MR and Mattei M (2021) Neogene tectono-stratigraphic evolution of the intermontane Tarom Basin: insights into basin filling and plateau building processes along the northern margin of the Iranian Plateau (Arabia-Eurasia Collision Zone). *Tectonics* **40**, e2020TC006254.

Pang KN, Chung SL, Zarrinkoub MH, Khatib MM, Mohammadi SS, Chiu HY, Chu CH, Lee HY and Lo CH (2013) Eocene-Oligocene post-collisional magmatism in the Lut-Sistan region, eastern Iran: magma genesis and tectonic implications. *Lithos* **180–181**, 234–51.

https://doi.org/10.1017/S0016756822001066 Published online by Cambridge University Press

Pearce JA (1982) Trace element characteristics of lavas from destructive plate boundaries. In *Orogenic Andesites and Related Rocks*. Chichester, England: John Wiley and Sons, 528–48.

Pearce JA, Harris NBW and Tindle AG (1984) Trace element discrimination diagrams for the tectonic interpretation of granitic rocks. *Journal of Petrology* **25**, 956–83.

Pearce JA, Stern RJ, Bloomer SH and Fryer P (2005) Geochemical mapping of the Mariana arc-basin system: implications for the nature and distribution of subduction components. *Geochemistry, Geophysics, Geosystems* **6**, Q07006.

Peccerillo A and Taylor SR (1976) Geochemistry of Eocene calc-alkaline volcanic rocks from the Kastamonu area, Northern Turkey. *Contributions to Mineralogy and Petrology* **58**, 63–81.

Rossetti F, Monié P, Nasrabady M, Theye T, Lucci F and Saadat M (2017) Early carboniferous subduction-zone metamorphism preserved within the Palaeo-Tethyan Rasht ophiolites (Western Alborz, Iran). *Journal of the Geological Society, London* **174**, 741–58.

Rossetti F, Nozaem R, Lucci F, Vignaroli G, Gerdes A, Nasrabadi M and Theye T (2015) Tectonic setting and geochronology of the Cadomian (Ediacaran-Cambrian) magmatism in Central Iran, Kuh-e-Sarhangi region (NW Lut Block). *Journal of Asian Earth Sciences* **102**, 24–44.

Rubatto D, Williams IS and Buick IS (2001) Zircon and monazite response to prograde metamorphism in the Reynolds Range, central Australia. *Contributions to Mineralogy and Petrology* **140**, 458–68.

Saccani E, Delavari M, Beccaluva L and Amini S (2010) Petrological and geochemical constraints on the origin of the Nehbandan ophiolitic complex (eastern Iran): implication for the evolution of the Sistan Ocean. *Lithos* **117**, 209–28.

Sahandi MR (1992) Geological Quadrangle Map of Iran, Dehsalm (Chah Vak) sheet (K9), scale 1: 250,000. Tehran: Geological Survey of Irān.

Samiee S, Karimpour MH, Ghaderi M, Haidarian Shahri MR, Klöetzli U and Santos JF (2016) Petrogenesis of subvolcanic rocks from the Khunik prospecting area, south of Birjand, Iran: geochemical, Sr-Nd isotopic and U-Pb zircon constraints. *Journal of Asian Earth Sciences* **115**, 170–82.

Şengör AM and Natal'in BA (1996) Turkic-type orogeny and its role in the making of the continental crust. *Annual Review of Earth and Planetary Sciences* **24**, 263–337.

Sepidbar F, Mirnejad H, Ma C and Moghadam HS (2018) Identification of Eocene-Oligocene magmatic pulses associated with flare-up in east Iran: timing and sources. *Gondwana Research* **57**, 141–56.

Sepidbar F, Shafaii Moghadam H, Zhang L, Li JW, Ma J, Stern RJ and Lin C (2019) Across-arc geochemical variations in the Paleogene magmatic belt of Iran. *Lithos* **344–345**, 280–96.

Shafaii Moghadam H, Griffin WL, Kirchenbaur M, Gare-Schnoberg D, Khedr MZ and Kimura JI (2018) Roll-back, extension and mantle upwelling triggered Eocene potassic magmatism in NW Iran. *Journal of Petrology* **59**, 1417–65.

Shafaii Moghadam H, Khademi M, Hu Z, Stern RJ, Santos JF and Wu Y (2015a) Cadomian (Ediacaran-Cambrian) arc magmatism in the ChahJam-Biarjmand metamorphic complex (Iran): magmatism along the northern active margin of Gondwana. *Gondwana Research* **27**, 439–52.

Shafaii Moghadam H, Khedr MZ, Arai S, Stern RJ, Gorbani G, Tamura A and Ottley CJ (2015b) Arc-related harzburgite-dunite-chromitite complexes in the mantle section of the Sabzevar ophiolite, Iran: a model for formation of podiform chromitites. *Gondwana Research* **27**, 575–93.

Shafaii Moghadam H, Li QL, Li XH, Stern RJ, Levresse G, Santos JF, Lopez Martinez M, Ducea MN, Ghorbani G and Hassannezhad A (2020) Neotethyan subduction ignited the Iran Arc and Backarc differently. *Journal of Geophysical Research: Solid Earth* **125**, e2019JB018460.

Shafaii Moghadam H and Stern RJ (2021) Subduction initiation causes broad upper plate extension: the Late Cretaceous Iran example. *Lithos* **398**, 106296.

Shafaii Moghadam H, Whitechurch H, Rahgoshay M and Monsef I (2009) Significance of Nain-Baft ophiolitic belt (Iran): short-lived, transtensional Cretaceous back-arc oceanic basins over the Tethyan subduction zone. *Comptes Rendus – Geoscience* **341**, 1016–28.

Shand SJ (1948) Eruptive rocks: their genesis, composition, classification, and their relation to ore deposits. *The Journal of Geology* **56**, 593–3.

Shomali ZH, Keshvari F, Hassanzadeh J and Mirzaei N (2011) Lithospheric structure beneath the Zagros collision zone resolved by non-linear teleseismic tomography. *Geophysical Journal International* **187**, 394–406.

Stacey JS and Kramers JD (1975) Approximation of terrestrial lead isotope evolution by a two-stage model. *Earth and Planetary Science Letters* **26**, 207–21.

Stampfli GM, Marcoux J and Baud A (1991) Tethyan margins in space and time. Palaeogeography, Palaeoclimatology, Palaeoecology 87, 373–409.

Sun S-S and McDonough W (1989) Chemical and isotopic systematics of oceanic basalts: implications for mantle composition and processes. *Geological Society of London, Special Publication* **42**, 313–45.

Tatsumi Y (2005) The subduction factory: how it operates in the evolving Earth. *GSA Today* **15**, 4–10.

Taylor SR and McLennan SM (1985) *The Continental Crust: Its Composition and Evolution*. Oxford: Blackwell, 312 pp.

Thieblemont D and Tegyey M (1994) Une discrimination géochimique des roches différenciées temoin de la diversité d'origine et de situation tectonique des magmas calco- alcalins. *Comptes Rendus – Académie des Sciences, Série II: Sciences de la Terre et des Planèetes* **319**, 87–94.

Tirrul R, Bell IR, Griffis RJ and Camp VE (1983) The Sistan suture zone of eastern Iran. *Geological Society of America Bulletin* **94**, 134–50.

Verdel C, Wernicke BP, Hassanzadeh J and Guest B (2011) A Paleogene extensional arc flare-up in Iran. *Tectonics* **30**, 1–20.

Vergés J, Saura E, Casciello E, Fernàndez M, Villaseñor A, Jiménez-Munt I and García-Castellanos D (2011) Crustal-scale cross-sections across the NW Zagros belt: implications for the Arabian margin reconstruction. *Geological Magazine* **148**, 739–61.

Vincent SJ, Allen MB, Ismail-Zadeh AD, Flecker R, Foland KA and Simmonds MD (2005) Insights from the Talysh of Azerbaijan into the Paleogene evolution of the South Caspian region. *Geological Society of America Bulletin* **117**, 1513–33.

Whitney DL and Evans BW (2010) Abbreviations for names of rock-forming minerals. *American Mineralogist* **95**, 185–7.

Willbold M and Stracke A (2010) Formation of enriched mantle components by recycling of upper and lower continental crust. *Chemical Geology* **276**, 188–97.

Wilson M (1989) *Igneous Petrogenesis: A Global Tectonic Approach*. London: Chapman and Hall, 466 pp.

Wu Y and Zheng Y (2004) Genesis of zircon and its constraints on interpretation of U-Pb age. *Chinese Science Bulletin* **49**, 1554–69.

Zanchetta S, Berra F, Zanchi A, Bergomi M, Caridroit M, Nicora A and Heidarzadeh G (2013) The record of the Late Palaeozoic active margin of the Palaeotethys in NE Iran: constraints on the Cimmerian orogeny. *Gondwana Research* **24**, 1237–66.

Zarrinkoub MH, Pang K-N, Chung S-L, Khatib MM, Mohammadi SS, Chiu H-Y and Lee H-Y (2012) Zircon U-Pb age and geochemical constraints on the origin of the Birjand ophiolite, Sistan suture zone, eastern Iran. *Lithos* **154**, 392–405.

Zhang Z, Xiao W, Ji W, Majidifard MR, Rezaeian M, Talebian M, Xiang D, Chen L, Wan B, Ao S and Esmaeili R (2018) Geochemistry, zircon U-Pb and Hf isotope for granitoids, NW Sanandaj-Sirjan zone, Iran: implications for Mesozoic-Cenozoic episodic magmatism during Neo-Tethyan lithospheric subduction. *Gondwana Research* **62**, 227–45.

Zindler A and Hart S (1986) Chemical geodynamics. *Annual Review of Earth and Planetary Sciences* **14**, 493–571.

https://doi.org/10.1017/S0016756822001066 Published online by Cambridge University Press